Mammary ductal epithelium controls cold-induced adipocyte thermogenesis

Luis Santos

Icahn School of Medicine at Mount Sinai

Douglas Arneson

University of California

Alexandra Alvarsson

Icahn School of Medicine at Mount Sinai

Karthickeyan Krishnan

University of California

Alessia Centzone

Université Libre de Bruxelles

Sanil Patel

Icahn School of Medicine at Mount Sinai

Shani Sadeh

Icahn School of Medicine at Mount Sinai   https://orcid.org/0000-0002-6892-7043

In Sook Ahn

University of California

Graciel Diamante

University of California

Ingrid Cely

University of California

Atul Butte

Bakar Institute for Computational Health Sciences, University of California, San Francisco
https://orcid.org/0000-0002-7433-2740

Cédric Blanpain

Université Libre de Bruxelles   https://orcid.org/0000-0002-4028-4322

Sarah Stanley

Icahn School of Medicine at Mount Sinai

Aldons Lusis

University of California Los Angeles   https://orcid.org/0000-0001-9013-0228

Xia Yang

University of California

Prashant Rajbhandari (✉ prashant.rajbhandari@mssm.edu)

Icahn School of Medicine at Mount Sinai   https://orcid.org/0000-0002-8146-3861

Biological Sciences - Article

Keywords:

Mammary ductal epithelium controls cold-induced adipocyte thermogenesis

Luis C. Santos[1,8], Douglas Arneson[2,5,8], Alexandra Alvarsson[1,8], Karthickeyan Chella Krishnan[3], Alessia Centzone[4], Sanil Patel[1], Shani Sadeh[1], In Sook Ahn[5], Graciel Diamante[5], Ingrid Cely[5], Atul J. Butte[2,6,7], Cédric Blanpain[5], Sarah A. Stanley[1], Aldons J. Lusis[3], Xia Yang[5], and Prashant Rajbhandari[1, 9]

[1]Diabetes, Obesity, and Metabolism Institute, Icahn School of Medicine at Mount Sinai, New York, NY USA
[2]Bakar Computational Health Sciences Institute, University of California, San Francisco, CA USA
[3]Department of Medicine/Division of Cardiology and Department of Human Genetics, University of California, Los Angeles, CA USA
[4]Laboratory of Stem Cells and Cancer, Université Libre de Bruxelles (ULB), Brussels, Belgium
[5]Department of Integrative Biology and Physiology and Bioinformatics Interdepartmental Program, University of California, Los Angeles, CA USA
[6]Department of Pediatrics, University of California, San Francisco, CA, USA
[7]Center for Data-Driven Insights and Innovation, University of California Health, Oakland, CA, USA

[8]Equal Contribution

[9]Corresponding author:

Prashant Rajbhandari PhD
Diabetes, Obesity, and Metabolism Institute
Department of Endocrinology and Bone Disease
Icahn School of Medicine at Mount Sinai
1 Gustave L. Levy Place
New York, NY 10029 USA
Office (212) 659-8653
E-mail: prashant.rajbhandari@mssm.edu

Main Figures: 4; Extended Data Figures: 4; Supplemental Movies: 2

ABSTRACT

Sympathetic activation during cold exposure increases adipocyte thermogenesis via expression of mitochondrial protein uncoupling protein 1 (UCP1)[1]. The propensity of adipocytes to express UCP1 is under a critical influence of the adipose microenvironment and varies among various fat depots[2-7]. Here we report that cold-induced adipocyte UCP1 expression in female mouse subcutaneous white adipose tissue (scWAT) is regulated by mammary gland ductal epithelial cells in the adipose niche. Single cell RNA-sequencing (scRNA-seq) show that under cold condition glandular alveolar and hormone-sensing luminal epithelium subtypes express transcripts that encode secretory factors involved in regulating adipocyte UCP1 expression. We term mammary duct secretory factors as "mammokines". Using whole-tissue immunofluorescence 3D visualization, we reveal previously undescribed sympathetic nerve-ductal points of contact and show that sympathetic nerve-activated mammary ducts limit adipocyte UCP1 expression via cold-induced mammokine production. Both *in vivo* and *ex vivo* ablation of mammary ductal epithelium enhances cold-induced scWAT adipocyte thermogenic gene program. The mammary duct network extends throughout most scWATs in female mice, which under cold exposure show markedly less UCP1 expression, fat oxidation, energy expenditure, and subcutaneous fat mass loss compared to male mice. These results show a previously uncharacterized role of sympathetic nerve-activated glandular epithelium in adipocyte thermogenesis. Overall, our findings suggest an evolutionary role of mammary duct luminal cells in defending glandular adiposity during cold exposure, highlight mammary gland epithelium as a highly active metabolic cell type, and implicate a broader role of mammokines in mammary gland physiology and systemic metabolism.

MAIN

The scWAT depots in female mice are mostly mammary gland WATs (mgWAT) which is highly heterogenous tissue consisting of adipocytes, preadipocytes, mesenchymal stem cells, immune cells, endothelial cells, SNS nerve fibers, and mammary epithelial cells forming a ductal structure. The epithelial cells are divided into myoepithelial/basal cells, and luminal cells, which can be luminal hormone sensing, or not[8]. In virgin female mice, the mammary gland already has ductal structures in the anterior and posterior scWAT and metabolic cooperativity between luminal ductal cells and stroma is known to be important for mammary gland function and development[8,9]. Profound changes in mammary ducts and adipocytes are seen during gestation, pregnancy, lactation, and post-involution[10,11]. The importance of adipocytes for mammary duct morphogenesis, the dedifferentiation of adipocytes during lactation, and reappearance during lactation post-involution, all suggest a dynamic homeostatic interplay between ductal luminal epithelial cells and adipocytes[11-13]. It is not clear, however, what paracrine signaling programs from mammary ducts regulate adipocyte metabolism and thermogenesis. Notably, our current-state-of knowledge of WAT thermogenesis and UCP1 expression is mostly based on male scWATs, which lacks mammary glandular epithelial cells. Importantly, besides the role of immune cells in the adipose microenvironment, the contribution of other cell types in controlling adipocyte UCP1 expression is still not clear.

To study cellular heterogeneity, inter-tissue communication, and cellular transcription dynamics in mgWAT in a thermogenic condition, we isolated the stromal vascular fraction (SVF) from the mgWAT of 10-week-old virgin female mice exposed to 24-hour cold (COLD, 4ºC) or room temperature (RT) and performed scRNA-seq (Fig. 1A). We obtained 12,222 cells and used Cell Ranger software from 10X Genomics for data processing and the R package Seurat[14] to

83   generate cell clusters and resolve their identities as previously described[15] (see Methods). We

84   integrated our dataset with eight other publicly available single cell datasets, from mammary gland

85   tissues including *Tabula Muris* and *Tabula Muris Senis*[16-19] : i) for cell type identification, ii) to

86   increase confidence in the projected cell type, iii) for sex and age differences, and iv) for mammary

87   gland development (Extended Data Fig. 1A, and Table 1). This integrated dataset allowed us to

88   precisely annotate various cell types present in mgWAT of female mice. Further subclustering of

89   our integrated dataset based on known cell type marker genes identified clusters of a) adipocyte

90   precursor cells (APCs), b) B cells, c) macrophages, d) T cells, e) endothelial cells, f) immune

91   precursor cells (IPC), g) dendritic cells (DC) , h) Schwann cells, i) myoepithelial cells (myoep),

92   and j) luminal-hormone sensing (Luminal-HS), luminal-alveolar (Luminal -AV), luminal-HS-AV,

93   and myoepithelial cells (Fig. 1B, Extended Data Fig. 1B and 1C).

94   To gain insight into the remodeling of stromal cells under adrenergic stress, we segregated

95   the cumulative tSNE-plot into RT and COLD treatment by animal replicate. The tSNE and dot

96   plots reveal global changes in relative proportions of SVF clusters between RT and COLD (Fig.

97   1C). Among all the clusters luminal cells showed significant differences in cell type percentages

98   (RT 1:7.2%, RT 2: 7.5%; COLD 1: 16.9%, COLD 2: 19.1%) and appeared to have large

99   differences in their global transcriptomic profiles in the t-SNE two-dimensional projection where

100   cells from RT and COLD were segregated (Fig. 1C). To quantitatively determine the

101   transcriptional impact of cold treatment on individual cell types, we characterized differentially

102   expressed genes as a function of cluster types and found a high degree of transcriptional variation

103   in luminal HS and AV under the cold conditions (Extended Data Fig. 1D). Further subclustering

104   of luminal epithelial cell types (luminal HS, luminal AV, and luminal HS-AV) revealed marked

105   differences in clustering at RT and COLD [20] (Fig. 1C and Extended Data Fig. 1D, 1E).

106   Luminal cell clusters showed remarkable transcriptional differences in cell clusters

107   between RT and cold, implicating a potential remodeling of the luminal epithelium upon cold

108   exposure (Fig. 1C, 1D and Extended Data Fig. 1D-1F). To probe for factors that are differentially

109   expressed in luminal cells under cold exposure, we performed differential gene expression (DEG)

110   analysis on RT and cold exposed luminal subclusters. We found upregulation of *Wnt4*, Adropin

111   (*Enho*), leucine rich alpha-2 glycoprotein (*Lrg1*), Diglyceride acyltransferase (*Dgat2*), haptoglobin

112   (*H*p), and angiopoietin-like 4 (*Angptl4*) in Luminal HS cells, lipocalin-2 (*Lcn2*), *Angptl4*, and

113   Apolipoprotein B editing complex (*Apobec3*) in Luminal AV cells, and *Lrg1*, neuregulin 4 (*Nrg4*),

114   ceruloplasmin (*Cp*), *Angptl4* in Luminal HS-AV cells (Fig. 1E-1G, Extended Data Fig. 1G). Many

115   of these genes (shown by red arrows in Fig. 1E-1G) encode secreted factors that play important

116   roles in local and systemic lipid metabolism[21-30]. t-SNE plots of normalized gene expression levels

117   for cold-induced mammokines in mgWAT (our study), male scWAT SVFs and mature

118   adipocytes[31] show that *Angptl4* is also expressed by most mature adipocytes; however, other cold-

119   induced mammokine genes showed relatively localized expression in ductal epithelial cell

120   adhesion molecule (*Epcam)+* cells (Extended Data Fig. 1G and 1H). Our RNAscope fluorescent

121   in situ hybridization (FISH) analysis showed a highly localized expression of mammokines *Enho,*

122   *Mfge8, Lrg1, Lcn2, Hp, Nrg4,* and *Wnt4* in *Epcam+* and *Krt8+* (luminal ductal epithelial markers)

123   in mammary ductal luminal cells (Fig. 1H).

124   Shifts in the luminal epithelium transcriptomic state with cold and localized expression of

125   beta-adrenergic receptors, *Adrb2* and *Adrb1* expression in luminal cells, suggests that these cells

126   may directly respond to cold-induced SNS activation[32-34] (Fig. 1C and Extended Data Fig. 1G). To

127   determine if duct epithelial cells are innervated by sympathetic nerves, we used Adipoclear, a

128   robust protocol based on immunolabeling-enabled three-dimensional imaging of solvent-cleared

129 organ iDISCO (22), for high-resolution, three-dimensional imaging of mammary tissue. We

130 analyzed the 3D distribution and density of a sympathetic marker, tyrosine hydroxylase (TH), and

131 its relationship to EPCAM+ mammary ductal cells in mgWAT from mice exposed to RT or cold.

132 Cold exposure caused prominent morphological changes in mammary ducts such as increased

133 EPCAM+ branching and terminal ductal bifurcations (Fig. 2A and Extended Data Fig. 2A), which

134 is consistent with data showing increased branch morphogenesis upon isoproterenol treatment[35].

135 Our data further reveal that nerve fibres are interwoven with mammary gland ducts and alveolar

136 structures in mgWATs (Supplementary Movie 1). However, we did not see an effect of cold

137 treatment on duct volume, nerve volume, or the ratio of duct-to-nerve volume (Fig. 2B). To

138 examine interactions between sympathetic innervation and mammary gland ducts in more detail,

139 we performed confocal imaging in six regions of the mgWAT fat pad from each of 6 RT and 6

140 cold-treated mice. Consistent with our scRNA-seq data, we saw a significant increase in EPCAM

141 staining in the ducts of cold-exposed mgWAT (Fig 2C and 2D). We also identified contacts

142 between TH+ fibres and EPCAM+ ducts (neuroductal points) with a trend to increased volume of

143 nerve contacts (normalized for duct volume) in cold-treated mice (p = 0.09, Fig S2F). Interestingly,

144 TH intensity, which has been reported to increase with sympathetic activation, was significantly

145 higher at the neuroductal points in cold exposed mgWAT compared to controls (Fig 2C, 2E, 2F

146 Supplementary Movie 2). Similarly, EPCAM intensity was also significantly elevated at

147 neuroductal points in keeping with local induction of expression. However, there were no

148 significant changes in duct or nerve volume or in TH intensity across the whole nerve volume

149 (Extended Data Fig 2C-2H). Taken together, our data show a significant remodelling of mammary

150 ducts and their contacts with sympathetic innervation upon cold exposure.

151   To explore the biological relevance of cold-induced increase in i) luminal subtype

152   population transcriptional state (Fig. 1) and ii) EPCAM intensity and SNS innervation of

153   mammary ducts (Fig. 2), we first purified EPCAM+ and EPCAM- cells from mgWAT of RT and

154   cold-exposed mice and then stained for EPCAM and CD49F for fluorescence-activated cell sorting

155   (FACS) analysis to probe for luminal cell population changes under cold stress. As shown in

156   Extended Data Fig. 3A, we noticed three distinct populations of cells that were EPCAM^{lo}CD49F^{lo}

157   (stromal), EPCAM^{hi}CD49F^{hi} (luminal), and EPCAM^{lo}CD49F^{hi} (basal) cells. Luminal cells were

158   only enriched in EPCAM+ purified cells and showed a cold-dependent increase in cell population

159   compared to RT conditions. We also noticed a marked reduction in the basal cell population upon

160   cold treatment in EPCAM+ selected cells, consistent with the scRNA-seq data in Fig. 1C

161   (myoepithelial cluster, RT: 2.15%, COLD: 0.65%). These data indicate a differential response to

162   cold stress by luminal and basal cells in ducal epithelium (Extended Data Fig. 3A). To test whether

163   luminal cells directly responded to SNS activation, we tested mammokine expression in isolated

164   primary EPCAM+ mgWAT that were either treated or not treated with isoproterenol. Cold-induced

165   mammokines showed increased expression upon isoproterenol (beta-adrenergic receptor agonist)

166   treatment (Extended Data Fig. 3B). To determine whether adrenergic-activated luminal cells are

167   involved in mgWAT adipose thermogenesis, we depleted EPCAM+ cells from mgWAT SVFs by

168   positive selection using magnetic cell sorting (MACS) and differentiated SVFs *ex vivo* with and

169   without ductal cells into beige adipocytes (Fig. 3A). Depletion of EPCAM+ cells from SVFs of

170   RT mgWAT potentiated expression of thermogenic genes such as *Ucp1*, *Cox8b, Ppargc1a* and

171   *Cidea* and this potentiation of thermogenic genes was markedly amplified in the cold-exposed

172   condition (Fig. 3A and Extended Data Fig 3C). To further test the crosstalk of epithelial cells and

173   adipocytes, we developed an *in vitro* co-culture system involving a controlled mixture of

174   adipogenic 10T1/2 cells with nontransformed mouse mammary gland (NMuMG cells) (derived

175   from "normal" mammary epithelium). Seeding density of as low as 2.5% NMuMG cells resulted

176   in a significant reduction of *Ucp1* and beiging potential of 10T1/2 cells compared to the pure

177   culture (Fig. 3B and Extended Data Fig. 3D-3F). The higher the fraction of NMuMG cells in the

178   co-culture, the lower the relative expression of *Ucp1* and other thermogenic genes such as *Cox8B*

179   and *Ppargc1a* measured by RT-qPCR (Fig. 3B). To test the *ex vivo* and *in vivo* role of ductal

180   epithelial cells in adipose thermogenesis, we compared aged-matched female mgWAT with three

181   complimentary ductal ablated models; i) estrogen receptor-alpha (ERa) knockout mice (*Esr1* KO),

182   ii) male mice which lack or possess only rudimentary glandular ducts, iii) inguinal (ducts) or

183   dorsolumbar (no ducts) portion of mgWAT from 5-week-old female mice. First, to test the role of

184   ductal cells in adipose thermogenesis, we isolated SVFs from male iWATs and female mgWATs

185   and differentiated them into beige adipocytes in the presence or absence of isoproterenol. We

186   found that SVFs from male iWATs show markedly higher beiging and isoproterenol-mediated

187   *Ucp1* expression compared to EPCAM+ SVFs from female mgWAT (Fig. 3C and Extended Data

188   Fig. 3G). In agreement with the ex vivo data, female mgWATs showed significantly less

189   expression of cold-induced thermogenic genes such as *Ucp1*, *Cox8b,* and *Ppargc1a* compared to

190   male iWATs (Fig. 3D). Since mgWATs make up almost all of the subcutaneous fat mass in female

191   mice, we reasoned that highly reduced adipocyte thermogenic gene expression could potentially

192   influence whole body energy metabolism. To test this, we performed indirect calorimetry on age-

193   matched male and female mice at RT and 24 hr cold exposure using a metabolic chamber. We

194   found that female mice showed highly reduced energy expenditure (EE), oxygen consumption

195   (VO2), and carbon dioxide production (VCO2) during cold exposure compared to male mice (Fig.

196   3E and Extended Data Fig. 3I). Female mice showed markedly higher respiratory exchange ratio

197 (RER) than males under cold exposure, indicating a decrease in cold-induced fat oxidation and the

198 possibility that mgWATs maintain adiposity under cold stress (Fig. 3E and Extended Data Fig.

199 3J). Generalized linear model (GLM)-based regression analyses showed a significant group and

200 interaction effect in RER between males and females based on fat mass as a covariate (Extended

201 Data Fig. 3J). We did not see significant differences in locomotor activities and food consumption

202 between the sexes (Extended Data Fig. 3K). These RER data were further supported by our

203 magnetic resonance imaging (MRI) body composition analysis which showed that male mice lose

204 significant body weight and fat mass during cold stress whereas females show no differences

205 before and after cold stress (Fig.3F and Extended Data Fig. 3H). Next, we compared the cold-

206 induced thermogenic gene expression program between WT and Estrogen Receptor-alpha (*Esr1*

207 KO) mice. *Esr1* KO mice are known to possess hypoplastic mammary ducts and remain

208 rudimentary throughout the life span of a female mouse[36]. As shown in Fig. 3G, cold-exposed *Esr1*

209 KO mice showed markedly increased expression of *Ucp1,* and other thermogenic genes compared

210 to WT control. In the 5 weeks after birth, mammary ducts are concentrated in the inguinal portion

211 closer to the nipple and are confined near the lymph node and virtually absent toward the

212 dorsolumbar region of the mgWAT, providing distinct anatomical regions within the mgWAT to

213 test the role of ductal epithelium in adipose thermogenesis[37]. 5-week-old female mice were

214 exposed to cold and inguinal and dorsolumbar regions were dissected to assess thermogenic

215 transcripts. *Epcam* transcripts were present only in the inguinal region, however, thermogenic

216 genes were mostly similar between inguinal and dorsolumbar region except for *Ucp1* where we

217 saw an increase in *Ucp1* levels in inguinal part (Fig. 3H). Chi et. al reported regional differences

218 between inguinal and dorsolumbar region and there could be a regional control of *Ucp1* expression

219 in 5-week-old mice independent of ductal cells[38]. However, consistent with our data, we noticed

220   significantly less expression of genes involved in lipid mobilization such as *Pnpla2* and *Hsl,* in

221   inguinal regions compared to dorsolumbar, indicating that the ductal epithelium is potentially

222   inhibiting cold-induced lipid mobilization. All these data point, for the first time, toward a possible

223   unique mechanism of SNS-activated mgWAT under cold stress to limit thermogenesis and

224   preserve adiposity.

225   Our results show a unique possible SNS-mediated crosstalk between mammary ductal cells

226   and adipocytes to control adipocyte thermogenesis. Our differentially expressed genes in

227   mammary ductal cells under adrenergic stimulation showed upregulation of genes that encode

228   factors such as Angptl4*,* Enho, Lrg1, and Lcn2, which are known to play inhibitory roles in

229   adipocyte thermogenesis. These factors also showed high enrichment in mammary *Epcam+* cells

230   by scRNA-seq and RNAscope in situ hybridization. Among these factors, *Lcn2* was previously

231   shown to inversely correlate with *Ucp1* expression in female gonadal WAT (gWAT)[24]. Female

232   gWATs, which lack mammary ducts, express exceedingly high levels of *Ucp1* compared to male

233   gWATs[24]. Reciprocally, we find that cold-stressed female mgWATs express high levels of *Lcn2*

234   and low levels of *Ucp1* compared to males (Fig. 3D and Extended Data Fig. 4A). The secretion of

235   Lcn2 by luminal AV and HS-AV cells could potentially be a mechanism of luminal cells to block

236   excess thermogenesis and preserve adiposity. Consistent with data in Fig.1 and Fig.3, both

237   isoproterenol treatment and cold exposure led to an increase in *Lcn2* levels in *Epcam+* mammary

238   ducts (Extended Data Fig. 4B). To test adrenergic-dependent expression of Lcn2 protein

239   expression in luminal cells, we used organoids from a genetic mouse model that is based on

240   doxycycline (Dox)-based tet-responsive diphtheria toxin A (DTA) system derived from

241   interbreeding two transgenic strains: (1) mice expressing the tetracycline-on (''tet-on'')

242   transcription factor rtTA under the control of the luminal epithelial cell-specific *Krt8* gene

243   promoter (K8rtTA); (2) mice expressing tet-responsive DTA (TetO-Cre) that can be activated in

244   the presence of Dox. This model enables luminal cell ablation in a temporally regulated manner.

245   Mammary duct organoids isolated from *K8*rtTA-DTA mice[39] show increases in Lcn2 protein

246   expression upon isoproterenol treatment and these increases were diminished upon Dox treatment

247   (Fig. 4A and Extended Fig. 4C-4H), showing a direct response of luminal cells to produce Lcn2.

248   To test the physiological role of Lcn2 in regulating mgWAT thermogenesis, we mimicked cold

249   induction of Lcn2 production in mgWAT by inducing Lcn2 exogenous expression specifically in

250   mgWAT of *Lcn2* KO mice by injecting adipoAAV-Lcn2 or adipoAAV-GFP[24] (See Methods). Our

251   unbiased bulk RNA-seq data from the mgWATs of adipoAAV-Lcn2 injected mice show that *Lcn2*

252   expression was not supraphysiological compared to controls (Fig. 4B). The volcano plot in Fig.

253   4B demonstrates that Lcn2 exogenous expression significantly decreased the expression of

254   thermogenic genes such as *Ucp1, Cidea, Ppara* and increased expression of adipogenic genes

255   including *Lep, Mmp12*[40,41], *Zfp423*[42], and Lbp[43]. Lcn2 overexpression also led to an increase in

256   *Aldh1a1,* which was recently shown to inhibit adipose thermogenesis by downregulating UCP1

257   levels[44,45]. We validated our RNA-seq data by directed qPCR in both Lcn2 reconstituted mgWAT

258   of *Lcn2* KO and WT mice (Fig. 4C) and treated beige differentiated SVFs isolated from *Lcn2* KO

259   mgWATs with and without recombinant Lcn2 (Extended Data Fig. 4I). Finally, to test the role of

260   Lcn2 under cold stress, female *Lcn2* KO and WT mice were exposed to cold (4°C) for 24 hr.

261   Compared to controls, cold-exposed *Lcn2* KO mice mgWAT showed more beiging/browning and

262   gene expression analysis showed a significant increase in thermogenic genes such as *Ucp1*

263   indicating that Lcn2 is potentially one of the limiting factors involved in regulating the propensity

264   of mgWAT to beige (Extended Data Fig. 4J). Overall, our scRNA-seq analysis and both our tissue-

265   specific gain-of-function and loss-of-function experimental data show Lcn2 as a factor expressed

266   in luminal cells that could function to inhibit thermogenesis and maintain adiposity in mgWAT

267   during cold-stress.

268   In summary, our studies have uncovered a direct inhibitory role of mammary duct luminal

269   cells in adipocyte *Ucp1* expression and thermogenic gene program. SNS fibers directly innervate

270   EPCAM+ luminal cells and adrenergic stimulation of luminal cells transduce expression of

271   mammokines such LCN2 that regulates *Ucp1* expression in mgWAT adipocytes under cold

272   exposure. Depletion of EPCAM+ luminal epithelial cells potentiate the capacity of ex vivo

273   differentiated mgWAT preadipocytes to express UCP1, and female mice with ductal epithelium

274   loss show higher cold-induced UCP1 expression compared to controls. Importantly, female mice

275   demonstrate significantly less scWAT adipocyte UCP1 expression compared to male mice under

276   cold exposure. Taken together, these findings provide a new insight into mammary gland biology,

277   expand our understanding of the role of adipose microenvironment in adipocyte UCP1 expression,

278   and reveal the potential of mammokines to regulate local and systemic energy homeostasis.

279

280   **METHODS**

281   **Animal Studies**

282   C57BL/6 WT male and female mice (#000664), *ESR1* KO (#004744), LCN2KO (#24630) were

283   acquired from Jackson Laboratory and maintained in a pathogen-free barrier-protected

284   environment (12:12 h light/dark cycle, 22°C-24°C) at the UCLA and Mount Sinai animal facilities.

285   The Krt8rtTA-TetO-DTA mouse model was described previously[39]. For the time course cold

286   exposure experiment, WT mice at 8-10 weeks of age were singly housed at 4°C room in a non-

287   bedded cage without food and water for first 6 h; thereafter food, water, and one cotton square

288   were added. For the 24 h harvest, 3 h before harvest, food, water, and cotton square were removed

289 and then mice were harvested. At the end of the experiment, mgWATs were resected for analysis.

290 For overexpression studies, recombinant adeno-associated virus serotype 8 (AAV8) expressing

291 LCN2 or GFP was generated and injected as described previously[24]. Indirect calorimetry was

292 performed using Promethion Systems (Sable Systems, Las Vegas, NV). Animals were placed

293 individually in chambers at ambient temperature (22.0 °C) for 21 hr followed by 24 hr cold (4.0

294 °C) with 12 hr light/dark cycles. Animals had free access to food and water. Respiratory

295 measurements were made in 5 min intervals after initial 7-9 hr acclimation period. Energy

296 expenditure was calculated from VO2 and RER using the Lusk equation, EE in Kcal/hr = (3.815

297 + 1.232 X RER) X VO2 in ml/min. Indirect calorimetry data were analyzed by CALR web-based

298 software[46]. Body composition (fat mass) was determined using EchoMRI Body Composition

299 Analyzer. Animal experiments were conducted in accordance with the Mount Sinai and UCLA

300 Institutional Animal Care and Research Advisory Committee.

301

302 **RNA-Seq**

303 RNA isolation, library preparation, and analysis were conducted as previously described[24]. Flash-

304 frozen mgWAT samples were homogenized in QIAzol (Qiagen, Germantown, MD), and following

305 chloroform phase separation, RNA was isolated according to the manufacturer's protocol using

306 miRNeasy columns (Qiagen, Germantown, MD). Libraries were prepared from extracted mgWAT

307 fat RNA (Agilent 2200 Tapestation eRIN >8.2) using KAPA Stranded mRNA-Seq Kit (cat

308 #KK8421, KAPA Biosystems, Wilmington, MA), per the manufacturers' instructions. The pooled

309 libraries were sequenced using an Illumina HiSeq4000 instrument with SE50bp reads (Illumina,

310 San Diego, CA). Reads were aligned to the mouse genome mm10 using STAR[47] or HISAT2[48]

311 aligner and quantified using the Bioconductor R packages as described in the RNA-Seq

312 workflow[49]. *P* values were adjusted using the Benjamini-Hochberg procedure of multiple

313 hypothesis testing[49].

314

Single cell isolation from SVF

316 Single cell SVF populations from adipose tissue were isolated as described previously[3,31]. The

317 fourth inguinal white adipose tissue (iWAT) depot mgWAT from mice exposed to cold stress

318 (4°C) or room temperature for 24 hr was dissected and placed on a sterile 6-well tissue culture

319 plate with ice-cold 1X DPBS. Excess liquid was removed from fat pads by blotting. Each tissue

320 was cut and minced with scissors and then placed in 15 ml conical tubes containing digestion

321 buffer (2 ml DPBS and Collagenase II at 3 mg/ml; Worthington Biochemical, Lakewood, NJ,

322 USA) for 40 min of incubation at 37°C with gentle shaking at 100 rpm. Following tissue digestion,

323 enzyme activity was stopped with 8 ml of resuspension media (DMEM/F12 with glutamax

324 supplemented with 15%FBS and 1% pen/strep; Thermo Scientific, CA). The digestion mixture

325 was passed through 100 μm cell strainer and centrifuged at 150 x g for 8 min at room temperature.

326 To remove red blood cells, the pellet was resuspended and incubated in RBC lysis buffer (Thermo

327 Scientific, CA) for 3 min at room temperature, followed by centrifugation at 150 x g for 8 min.

328 The pellet was then resuspended in resuspension media and again spun down at 150 x g for 8 min.

329 The cell pellet was resuspended in 1 ml of 0.01% BSA (in DPBS) and passed through a 40 μm cell

330 strainer (Fisher Scientific, Hampton, NH, USA) to discard debris. Cell number was counted for

331 10X Genomics single cell application.

332

SVF single cell barcoding and library preparation

334 To yield an expected recovery of 4000-7000 single cells, an estimated 10,000 single cells per

335 channel were loaded onto Single Cell 3' Chip (10X Genomics, CA). The Single Cell 3' Chip was

336 placed on a 10X Genomics instrument to generate single cell gel beads in emulsion (GEMs).

337 Chromium Single Cell 3' v3 Library and Cell Bead Kits were used according to the manufacturer's

338 instructions to prepare single cell RNA-Seq libraries.

339

340 **Illumina high-throughput sequencing libraries**

341 Qubit Fluorometric Quantitation (ThermoFisher, Canoga Park, CA, USA) was used to quantify

342 the 10X Genomics library molar concentration and a TapeStation (Aligent, Santa Clara, CA, USA)

343 was used to estimated library fragment length. Libraires were pooled and sequenced on an Illumina

344 HiSeq 4000 (Illumina, San Diego, CA, USA) with PE100 reads and an 8 bp index read for

345 multiplexing. Read 1 contained the cell barcode and UMI and read 2 contained the single cell

346 transcripts.

347

348 **Single cell data pre-processing and quality control**

349 To obtain digital gene expression matrices (DGEs) in sparse matrix representation, paired end

350 reads from the Illumina HiSeq 4000 were processed and mapped to the mm10 mouse genome

351 using 10X Genomics' Cell Ranger v3.0.2 software suite. Briefly, .bcl files from the UCLA Broad

352 Stem Cell Research Center sequencing core were demultiplexed and converted to fastq format

353 using the 'mkfastq' function from Cell Ranger. Next, the Cell Ranger 'counts' function mapped

354 reads from fastq files to the mm10 reference genome and tagged mapped reads as either exonic,

355 intronic, or intergenic. Only reads which aligned to exonic regions were used in the resulting

356 DGEs. After combining all four sample DGEs into a single study DGE, we filtered out cells with

357   (1) UMI counts < 700 or > 30,000, (2) gene counts < 200 or > 8,000, and (3) mitochondrial gene

358   ratio > 10%. This filtering resulted in a dataset consisting of 42,052 genes across 12,222 cells, with

359   approximately 2,300 – 4,650 cells from each sample. A median of 2,411 genes and 7,252

360   transcripts were detected per cell.

361

362   **Identification of cell clusters**

363   To achieve high resolution cell type identification and increased confidence in our cell type

364   clustering we brought in external publicly available single cell data from SVF and mammary

365   tissues. Specifically, we included single cell data from 9 datasets comprising 91,577 single cells

366   from the mammary gland and multiple adipose depots, across 4 different single cell platforms

367   (**Table 1**). These external datasets and the SVF data from this study were all independently

368   normalized using sctransform[50] and integrated using Seurat[51,52] v3.1.5. The single cell expression

369   profiles were projected into two dimensions using UMAP[53] or tSNE[54] and the Louvain[55] method

370   for community detection was used to assign clusters. This integrated data was only used to identify

371   and define the cell types. All plots which are not explicitly designated as integrated with at least

372   one external dataset and all downstream analyses (e.g. differential expression analyses) were

373   conducted on non-integrated data to retain the biological effect of the cold treatment. Visualization

374   of the non-integrated data was conducted on a subsampled dataset where all samples had the same

375   number of cells to give an equal weight to each sample, however, all downstream analyses (e.g.

376   differential expression analyses) leveraged the full dataset.

Cell #	Tissue	Sex	Condition	Technology	Name	Source
22,800	BAT, EPI, ING)	M	SVF	Drop-Seq	Broad SVF	Broad Single Cell Portal[56]

25,010	Mammary	F	NP, G, L, PI	10X Genomics	MammaryEpi	GSE106273 [57]
14,927	Mammary	F	NP, G, L, PI	Microwell-seq	MouseCellAtlas	figshare[58,59]
4,481	Mammary	F	N/A	10X Genomics	TM.Mammary.10X	figshare[17,60]
2,405	Mammary	F	N/A	FACS + Smart-seq2	TM.Mammary.FACS	figshare[17,60]
4,967	SVF (BAT, GAT, MAT, SCAT)	F, M	N/A	FACS + Smart-seq2	TM.SVF.FACS	figshare[17,60]
3,132	Mammary	F	Age (3m, 18m, 21m)	FACS + Smart-seq2	TS.Mammary.FACS	figshare[18,61]
5,080	SVF (BAT, GAT, MAT, SCAT)	F, M	Age (18m, 21m, 30m)	10X Genomics	TS.SVF.10X	figshare[18,61]
8,775	SVF (BAT, GAT, MAT, SCAT)	F, M	Age (3m, 18m, 24m)	FACS + Smart-seq2	TS.SVF.FACS	figshare[18,61]

377

378 **Table 1: Publicly available single cell datasets used in this study**

379 BAT – brown adipose tissue, EPI – epididymal white adipose tissue, ING – inguinal white adipose

380 tissue, NP - nulliparous, G - gestation, L – lactation, PI - post involution, GAT – gonadal adipose

381 tissue, MAT – mesenteric adipose tissue, SCAT – subcutaneous adipose tissue

382

383 **Cell type-specific gene expression signatures**

384 Cell type-specific gene expression signatures were generated by identifying genes with expression

385 levels two-fold greater (adjusted p-values < 0.05) than all other cell types. To ensure consistency

386 across samples, Seurat's FindConservedMarkers function (Wilcoxon rank sum test with a meta p-

387 value) was applied across each sample.

388

Resolving cell identities of the cell clusters

390 To identify the cell type identity of each cluster, we used a curated set of canonical marker genes

391 derived from the literature (**Supplementary Table 1**) to find distinct expression patterns in the

392 cell clusters. Clusters which uniquely expressed known marker genes were used as evidence to

393 identify that cell type. Cell subtypes which did not express previously established markers were

394 identified by general cell type markers and novel markers obtained with Seurat's

395 FindConservedMarkers function were used to define the cell subtype.

396

Differential gene expression analysis

398 Within each identified cell type, cold treated and room temperature single cells were compared for

399 differential gene expression using Seurat's FindMarkers function (Wilcoxon rank sum test) in a

400 manner similar to Li et al.[19]. Differentially expressed genes were identified using two criteria: (i)

401 an expression difference of >= 1.5-fold and adjusted p-value < 0.05 in a grouped analysis between

402 room temperature mice (n = 2) and cold treated mice (n = 2); (ii) an expression difference of >=

403 1.25 fold and consistent fold change direction in all 4 possible pairwise combinations of cold-

404 treated vs room temperature mice.

405

Pathway enrichment analysis

407 Pathway enrichment analysis was conducted on the differentially expressed genes from each cell

408 type using gene sets from KEGG[62], Reactome[63], BIOCARTA[64], GO Molecular Functions[65], and

409 GO Biological Processes[65]. Prior to enrichment, mouse gene names were converted to human

410 orthologues. Enrichment of pathways was assessed with a Fisher's exact test, followed by multiple

411   testing correction with the Benjamini-Hochberg method. Gene set enrichments with FDR < 0.05

412   were considered statistically significant.

413

414   **Real time qPCR**

415   Total RNA was isolated using TRIzol reagent (Invitrogen) and reverse transcribed with the iScript

416   cDNA synthesis kit (Biorad). cDNA was quantified by real-time PCR using SYBR Green Master

417   Mix (Diagenode) on a QuantStudio 6 instrument (Themo Scientific, CA). Gene expression levels

418   were determined by using a standard curve. Each gene was normalized to the housekeeping gene

419   36B4 and was analyzed in duplicate. Primers used for real-time PCR are previously described[3,31]

420   and presented in Table 2.

421

422   **RNAScope Fluorescence in situ hybridization (FISH)**

423   mgWAT from RT or cold exposed mice (Jackson Laboratory, #000664) was fixed in 10% formalin

424   overnight, embedded with paraffin, and sectioned into unstained, 5 μm-thick sections. Sections

425   were baked at 60°C for 1 hour, deparaffinized, and baked again at 60°C for another hour prior to

426   pre-treatment. The standard pre-treatment protocol was followed for all sectioned tissues. *In situ*

427   hybridization was performed according to manufacturer's instructions using the RNAscope

428   Multiplex Fluorescent Reagent Kit v2 (#323136, Advanced Cell Diagnostics [ACD], Newark,

429   CA). Opal fluorophore reagent packs (Akoya Biosciences, Menlo Park, CA) for Opal 520

430   (FP1487A), Opal 570 (FP1488A), Opal 620 (FP1495A), and Opal 690 (FP1497A) were used at a

431   1:1000 dilution in TSA buffer (#322809, ACD). RNAscope probes from ACD were used for the

432   following targets: EPCAM (#418151), ENHO (#873251), LRG1 (#423381), LCN2 (#313971), HP

433   (#532711), WNT4 (#401101), NRG4 (#493731), KRT8 (#424528), and MFGE8 (#408778).

434 Slides were mounted with ProLong Diamond Antifade Mountant with DAPI (P36962, Life

435 Technologies, Carlsbad, CA). Fluorescent signals were captured with the 40x objective lens on a

436 laser scanning confocal microscope LSM880, (Zeiss, White Plains, NY).

437

438 **Fluorescent-activated cell sorting (FACS)**

439 Mammary gland white adipose tissue (mgWAT) from RT or cold exposed mice (Jackson

440 Laboratory, #000664) was dissected, cut, minced, and digested with collagenase D (5 mg/mL,

441 #11088882001, Roche, Germany) and dispase (2 mg/mL, #17105041, Gibco, Grand Island, NY)

442 over 40 min at 37°C with gentle shaking at 100 RPM. Enzymatic digestion was stopped with

443 DMEM/15% FBS and the cell suspension was filtered through a 100 μm nylon mesh cell strainer,

444 and centrifuged for 10 minutes at 700 x g. SVF pellet was resuspended in 1 mL Red Blood Cell

445 lysis buffer (#41027700, Roche, Germany) and incubated for 5 minutes at room temperature. Cell

446 suspension was diluted in 4 mL DPBS and filtered through a 40 μm nylon mesh cell strainer and

447 centrifuged for 10 minutes at 700 x g. Single cell suspension was blocked for 10 minutes on ice in

448 500 μL DPBS/5% BSA (blocking buffer), centrifuged for 10 min at 700 x g, resuspended in 200

449 μL of DBPS/0.5% BSA (FACS buffer) solution containing the desired antibody mix, and

450 incubated for 1 hour at 4°C in the dark with gentle rotation. Antibody-stained samples were washed

451 with 800 μL FACS buffer, centrifuged 10 minutes at 700 x g, and resuspended in FACS buffer

452 containing DAPI (at 1 ug/mL). Flow cytometry analysis was performed on a BD FACS Canto II

453 (BD Biosciences, San Jose, CA) and results analyzed on FCS Express software (DeNovo Software,

454 Pasadena, CA). Fluorescently-tagged anti-mouse antibodies (BioLegend, San Diego, CA) were

455 used to label cell surface markers for flow cytometry analysis: EPCAM-FITC (clone G8.8,

456 #118207), Sca-1-APC (Ly6, clone E13-161.7, #122512), CD49f-APC (clone GoH3, #313616).

457 For flow cytometry analysis, negative selection of CD45-expressing cells using CD45 microbeads

458 (#130052301) was performed immediately prior to the EPCAM positive selection protocol

459 described above.

460

461 **Isolation, selection, and *ex vivo* treatment of EPCAM-positive cells**

462 MACS microbeads (Miltenyi Biotec, Auburn, CA) were used for immuno-magnetic labeling

463 positive selection of EPCAM-expressing cells (anti-CD326, #130105958). Before magnetic

464 labeling, a single-cell suspension from the stromal vascular fraction of female mouse iWAT was

465 prepared in MACS buffer, i.e. PBS, pH 7.2, 0.5% bovine serum albumin (#A7030, SIGMA, St.

466 Louis, MO) and 2 mM EDTA, filtered through a MACS pre-separation 30 µm nylon mesh

467 (#130041407) to remove cell clumps. Then, for magnetic labeling of EPCAM-expressing cells, 10

468 µL of EPCAM microbeads were added per $1x10^7$ total cells in 100 uL buffer, incubated for 15

469 minutes with rotation at 4°C, washed with 1 mL buffer, centrifuged at 700 x *g* for 5 minutes,

470 resuspended in 500 µL buffer, and added to a pre-equilibrated MACS LS column (#130042401)

471 in the magnetic field of a MACS separator (#130042302). Unlabeled EPCAM-negative cells were

472 collected in the flow-through with three subsequent washes. The column was removed from the

473 magnetic field, 5 mL of MACS buffer were added to the column, and the magnetically-labeled

474 EPCAM-positive cells retained in the column were collected by flushing the cells down the column

475 with a plunger. Finally, EPCAM-negative and EPCAM-positive cell populations were centrifuged

476 at 700 x *g* for 5 minutes, resuspended in DMEM/F12 with glutamax supplemented with 15% FBS

477 and 1% pen/strep (Thermo Scientific, CA) and plated on Collagen I-coated 12-well tissue culture

478 plates (#354500, Corning, Kennebunk, ME). Media was replaced every other day during 6 days,

479 followed by cell lysis with Tryzol for phenol/chloroform RNA extraction, and RT-qPCR analysis.

Adipocyte differentiation and treatments

10T1/2 or SVF from the 4th inguinal (iWAT) mgWAT was isolated from 8 week old female *Lcn2*-null mice, respectively. 10T1/2 cells were maintained as previously described[3]. The pre-iWAT cells were maintained in Dulbecco's Modified Eagle Medium: Nutrient Mixture F-12 (DMEM/F12) supplemented with 1% glutamax, 10% fetal calf serum and 100 U/ml of both penicillin and streptomycin (basal media). Two days after plating (day 0), when the cells reached nearly 100% confluency, the cells were treated with an induction media containing basal media supplemented with 4 μg/mL insulin, 0.5 mM IBMX, 1 μM dexamethasone, and 1 μM rosiglitazone. After 48 h, the cells were treated with a maintenance media containing the basal media supplemented with 4 μg/mL insulin, and 1 μM rosiglitazone, with a media change every 2 days until day 10. For qPCR, differentiated iWAT cells were treated with 1 μg/ml recombinant LCN2 (Sino Biological Inc.) or differentiated 10T1/2 cells were treated with LRG1 (R&D Systems) for 24 h and then treated with isoproterenol (Sigma) for 6 h after which RNA was collected.

iDISCO and Adipoclear tissue labelling and clearing

Sample collection

Immediately after cold exposure mice were anaesthetized with isoflurane (3%) and perfused with heparinized saline followed by 4% paraformaldefyde (PFA) (Electron Microscopy Sciences, Hatfield, PA, USA). Fat pads were carefully dissected and postfixed overnight in 4% PFA at 4°C. On the following day the tissue was washed 3 times in PBS before proceeding with the optical clearing protocol.

Optical clearing

Whole-mount staining and clearing was performed using the Adipo-Clear protocol as previously described[1]. Dissected fat pads were dehydrated at room temperature (RT) with a methanol/B1n buffer (0.3 M glycine, 0.1% Triton X-100 in H_2O, pH 7) gradient (20%, 40%, 60%, 80%, 100%), incubated 3 times (1h, o/n, 2h) in 100% dichloromethane (DCM) (Sigma-Aldrich, St. Louis, MO, USA) to remove hydrophobic lipids, washed twice in 100% methanol, and bleached in 5% H_2O_2 overnight at $4^{\circ}C$ to reduce tissue autofluorescence. Fat pads were then rehydrated with a methanol/B1n buffer gradient (80%, 60%, 40%, 20%) and then washed twice in 100% B1n buffer (1h, o/n). Primary antibodies (EPCAM: 1:250; TH: 1:500) were diluted in modified PTxwH (PBS with 0.5% Trixon X-100, 0.1% Tween-20, 2 µg/ml heparin, as previously described[66] and applied for 6 days at $37^{\circ}C$. Following 5 washes with modified PTxwH over 1 day with the last wash performed overnight, secondary antibodies were diluted in modified PTxwH (1:500) and samples incubated for 6 days at $37^{\circ}C$. Samples were washed 5 times over 1 day in modified PTxwH at $37^{\circ}C$, 5 times over 1 day in PBS at RT, embedded in 1% agarose, dehydrated with a methanol gradient in H_2O (12%, 50%, 75%, 100%), washed 3 times for 1 hr in 100% methanol followed by 3 times for 1 hr in DCM, before being transferred to dibenzylether (DBE) (Sigma-Aldrich) to clear.

Imaging

Z-stacked optical sections of whole fat pads were acquired with an Ultramicroscope II (LaVision BioTec, Bielefeld, Germany) at a 1.3x magnification with a 4 µm step size and dynamic focus with a maximum projection filter. Samples were then imaged in glass-bottom µ-dishes (81158, Ibidi, Gräfelfing, Germany) using an inverted Zeiss LSM 710 confocal microscope with a 10x (NA: 0.3) objective and a step size of 5 µm.

Image analysis

Imaris versions 9.6.0-9.7.2 (Bitplane AG, Zürich, Switzerland) were used to create digital surfaces covering ducts, TH+ innervation and total sample volume (1.3x light sheet images and 10x confocal images) to automatically determine volumes and intensity data. Volume reconstructions were performed using the surface function with local contrast background subtraction. For detection of EPCAM+ ducts in 1.3x light sheet images, a smoothing factor of 5 µm was used and the threshold factor was set to correspond to the largest duct diameter in each sample. For detection of TH+ nerves in 1.3x light sheet images, a smoothing factor of 3 µm and a threshold factor of 80 µm were used. For detection of EPCAM+ ducts in 10x confocal images, a smoothing factor of 3.35 µm was used and a threshold factor corresponding to the diameter of the thickest duct wall in each sample was used. For detection of TH+ nerves in 10x confocal images, a smoothing factor of 2 µm and a threshold factor of 5 µm were used. In 10x confocal images, nerve/duct interactions were defined by masking the TH channel using the TH+ nerve surface to remove any background, and then masking it again using the EPCAM+ duct surface. This process revealed TH+ innervation overlapping with EPCAM+ staining. A new surface was created to cover this overlapping TH+ innervation using a smoothing factor of 2 µm and a threshold factor of 5 µm.

Statistical analyses

Data are shown as mean±S.E.M. Distribution was assessed by Shapiro-Wilk test. Significance was determined by a two-tailed unpaired *t* test (parametric distribution) or by a Mann-Whitney test (non-parametric distribution). Significance was set at an alpha level of 0.05.

Mammary gland organoids culture

For organoid culture, we used a previously published protocol[67]. In brief, fat pads of 8–9-week-old K8rtTA/TetO-DTA[39] virgin female mice were dissected and the lymph nodes removed.

549 Tissues were briefly washed in 70% ethanol and manually chopped into 1 mm^3 pieces. The finely

550 minced tissue was transferred to a digestion mix consisting of serum-free Leibovitz's L15 medium

551 (Gibco) containing 3 mg ml^{-1} collagenase A (Sigma) and 1.5 mg ml^{-1} trypsin (Sigma). This was

552 incubated for 1 hr at 37 °C to liberate epithelial tissue fragments ('organoids'). Isolated organoids

553 were mixed with 50 µl of phenol-red-free Matrigel (BD Biosciences) and seeded in 24-well plates.

554 The basal culture medium contained phenol-red-free DMEM/F-12 with penicillin/streptomycin,

555 10 mM HEPES (Invitrogen), Glutamax (Invitrogen), N2 (Invitrogen) and B27 (Invitrogen). The

556 basal medium was supplemented with Nrg1 (100 ng ml^{-1}, R&D), Noggin (100 ng ml^{-1}, Peprotech)

557 and R-spondin 1 (100 ng ml^{-1}, R&D). Then, 500 µl supplemented basal culture medium was added

558 per well and organoids were maintained in a 37 °C humidified atmosphere under 5% CO_2. After

559 one week in culture, mammary organoids were released from the Matrigel by breaking the matrix

560 with a P1000 pipette on ice. After 2–3 passages of washing and centrifugation at 1,500 rpm (140g)

561 for 5 min at 4 °C, mammary cells were resuspended in Matrigel, seeded in 24-well plates and

562 exposed to the previously described culture conditions. Organoids were treated either with 10 µg

563 ml^{-1} of DOX to promote luminal cell ablation or with 10µM of isoproterenol (Sigma) for 6 hr.

564 After 6 hr treatment, organoids were collected from Matrigel as mentioned before to perform

565 further analysis.

566 **RNA extraction and quantitative real-time PCR in organoid samples**

567 To perform RNA extraction, isolated organoids were collected into kit lysis buffer. RNA was

568 extracted with Qiagen RNeasy Micro Kit. After nanodrop RNA quantification and analysis of

569 RNA integrity, purified RNA was used to synthesize the first-strand cDNA in a 30 µl final volume,

570 using Superscript II (Invitrogen) and random hexamers (Roche). Genomic contamination was

571 detected by performing the same procedure without reverse transcriptase. Quantitative PCR

572   analyses were performed with 1 ng of cDNA as template, using FastStart Essential DNA green

573   master (Roche) and a Light Cycler 96 (Roche) for real-time PCR system. Relative quantitative

574   RNA was normalized using the housekeeping gene Gapdh. Analysis of the results was performed

575   using Light Cycler 96 software (Roche) and relative quantification was performed using the ddCt

576   method using Gapdh as a reference.

577

578   **Immunofluorescence in organoid samples**

579   For immunofluorescence, collected organoids were pre-fixed in 4% PFA for 30 min at RT. Pre-

580   fixed organoids were washed in 2%FBS-PBS, embedded in OCT and kept at -80°C. Sections of 4

581   µm were cut using a HM560 Microm cryostat (Mikron Instruments). Tissue sections were

582   incubated in blocking buffer (BSA 1%, HS 5%, Triton-X 0.2% in PBS) for 1 hr at RT. The different

583   primary antibodies were incubated overnight at 4 °C. Sections were then rinsed in PBS and

584   incubated with the corresponding secondary antibodies diluted at 1:400 in blocking buffer for 1 hr

585   at RT. The following primary antibodies were used: rat anti-K8 (1:1,000, Troma-I, Developmental

586   Studies Hybridoma Bank, University of Iowa), rabbit anti-EPCAM (1:1,000, ab71916, Abcam),

587   goat anti-Lcn2 (1:50, AF1857, R&D). The following secondary antibodies, diluted 1:400, were

588   used: anti-goat (A11055) conjugated to Alexa Fluor 488 (Invitrogen), anti-rat (712-295-155)

589   rhodamine Red-X and anti-rabbit (711-605-152) Cy5 (Jackson ImmunoResearch). Nuclei were

590   stained with Hoechst solution (1:2,000) and slides were mounted in DAKO mounting medium

591   supplemented with 2.5% DABCO (Sigma).

592
593   **Conflict of Interests (COI)**

594   AJB is a co-founder and consultant to Personalis and NuMedii; consultant to Samsung, Mango

595   Tree Corporation, and in the recent past, 10 × Genomics, Helix, Pathway Genomics, and Verinata

616 **Acknowledgements**

627

628 **Contributions**

629 D.A. performed all the scRNA-seq data analysis under the supervision of X.Y. L.C.S. performed

630 most of the biological experiments under the supervision of P.R. A.A. performed iDISCO and data

631 analysis under the supervision of S.A.S. K.C.K performed LCN2 related animal experiments under

632 the supervision of A.J.L. A.C.S performed organoid experiments under the supervision of C.B.

633 S.P. performed RNAscope and EPCAM cells isolation experiments under supervision of L.C.S

634 and P.R. S.S. performed indirect calorimetry and body composition studies under the supervision

635 of P.R.. I.S.A, G.D., and I.C., prepared single cell suspensions of mgWAT SVFs under the

636 supervision of P.R. and X.Y.. P.R. conceived the project and wrote the manuscript with help from

637 A.J.B., C.B., S.A.S, A.J.L., and X.Y.

638

639

REFERENCES

1   Chi, J. *et al.* Three-Dimensional Adipose Tissue Imaging Reveals Regional Variation in Beige Fat Biogenesis and PRDM16-Dependent Sympathetic Neurite Density. *Cell Metab* **27**, 226-236 e223, doi:10.1016/j.cmet.2017.12.011 (2018).

2   Zhang, F. *et al.* An Adipose Tissue Atlas: An Image-Guided Identification of Human-like BAT and Beige Depots in Rodents. *Cell Metab* **27**, 252-262.e253, doi:10.1016/j.cmet.2017.12.004 (2018).

3   Rajbhandari, P. *et al.* IL-10 Signaling Remodels Adipose Chromatin Architecture to Limit Thermogenesis and Energy Expenditure. *Cell* **172**, 218-233 e217, doi:10.1016/j.cell.2017.11.019 (2018).

4   Knights, A. J., Wu, J. & Tseng, Y.-H. The Heating Microenvironment: Intercellular Cross Talk Within Thermogenic Adipose Tissue. *Diabetes* **69**, 1599, doi:10.2337/db20-0303 (2020).

5   Li, J. *et al.* Neurotensin is an anti-thermogenic peptide produced by lymphatic endothelial cells. *Cell Metab* **33**, 1449-1465.e1446, doi:10.1016/j.cmet.2021.04.019 (2021).

6   Hu, B. *et al.* γδ T cells and adipocyte IL-17RC control fat innervation and thermogenesis. *Nature* **578**, 610-614, doi:10.1038/s41586-020-2028-z (2020).

7   Wang, Q. *et al.* IL-27 signalling promotes adipocyte thermogenesis and energy expenditure. *Nature*, doi:10.1038/s41586-021-04127-5 (2021).

8   Gjorevski, N. & Nelson, C. M. Integrated morphodynamic signalling of the mammary gland. *Nat Rev Mol Cell Biol* **12**, 581-593, doi:10.1038/nrm3168 (2011).

9   McNally, S. & Martin, F. Molecular regulators of pubertal mammary gland development. *Ann Med* **43**, 212-234, doi:10.3109/07853890.2011.554425 (2011).

10   Inman, J. L., Robertson, C., Mott, J. D. & Bissell, M. J. Mammary gland development: cell fate specification, stem cells and the microenvironment. *Development* **142**, 1028-1042, doi:10.1242/dev.087643 (2015).

11   Wang, Q. A. & Scherer, P. E. Remodeling of Murine Mammary Adipose Tissue during Pregnancy, Lactation, and Involution. *J Mammary Gland Biol Neoplasia* **24**, 207-212, doi:10.1007/s10911-019-09434-2 (2019).

12   Landskroner-Eiger, S., Park, J., Israel, D., Pollard, J. W. & Scherer, P. E. Morphogenesis of the developing mammary gland: stage-dependent impact of adipocytes. *Dev Biol* **344**, 968-978, doi:10.1016/j.ydbio.2010.06.019 (2010).

13   Wang, Q. A. *et al.* Reversible De-differentiation of Mature White Adipocytes into Preadipocyte-like Precursors during Lactation. *Cell Metab* **28**, 282-288 e283, doi:10.1016/j.cmet.2018.05.022 (2018).

14   Butler, A., Hoffman, P., Smibert, P., Papalexi, E. & Satija, R. Integrating single-cell transcriptomic data across different conditions, technologies, and species. *Nat Biotechnol* **36**, 411-420, doi:10.1038/nbt.4096 (2018).

15   Arneson, D. *et al.* Single cell molecular alterations reveal target cells and pathways of concussive brain injury. *Nat Commun* **9**, 3894, doi:10.1038/s41467-018-06222-0 (2018).

16   Bach, K. *et al.* Differentiation dynamics of mammary epithelial cells revealed by single-cell RNA sequencing. *Nat Commun* **8**, 2128, doi:10.1038/s41467-017-02001-5 (2017).

17   Tabula Muris, C. *et al.* Single-cell transcriptomics of 20 mouse organs creates a Tabula Muris. *Nature* **562**, 367-372, doi:10.1038/s41586-018-0590-4 (2018).

684   18   Tabula Muris, C. A single-cell transcriptomic atlas characterizes ageing tissues in the
685   mouse. *Nature* **583**, 590-595, doi:10.1038/s41586-020-2496-1 (2020).
686   19   Li CM, S. H., Tsiobikas C, Selfors L, Chen H, Gray GK, Oren Y, Pinello L, Regev A,
687   Brugge JS. Aging-associated alterations in the mammary gland revealed by single-cell
688   RNA sequencing. *bioRxiv* (2019).
689   20   Li, C. M.-C. *et al.* Aging-Associated Alterations in Mammary Epithelia and Stroma
690   Revealed by Single-Cell RNA Sequencing. *Cell Reports* **33**, 108566,
691   doi:https://doi.org/10.1016/j.celrep.2020.108566 (2020).
692   21   Aryal, B. *et al.* Absence of ANGPTL4 in adipose tissue improves glucose tolerance and
693   attenuates atherogenesis. *JCI Insight* **3**, doi:10.1172/jci.insight.97918 (2018).
694   22   De Keyser, J., De Backer, J. P., Ebinger, G. & Vauquelin, G. Regional distribution of the
695   dopamine D2 receptors in the mesotelencephalic dopamine neuron system of human brain.
696   *J Neurol Sci* **71**, 119-127, doi:10.1016/0022-510x(85)90041-3 (1985).
697   23   Arner, E. *et al.* Ceruloplasmin is a novel adipokine which is overexpressed in adipose tissue
698   of obese subjects and in obesity-associated cancer cells. *PLoS One* **9**, e80274,
699   doi:10.1371/journal.pone.0080274 (2014).
700   24   Chella Krishnan, K. *et al.* Sex-specific metabolic functions of adipose Lipocalin-2. *Mol
701   Metab* **30**, 30-47, doi:10.1016/j.molmet.2019.09.009 (2019).
702   25   Sun, W. Y. *et al.* Lipocalin-2 derived from adipose tissue mediates aldosterone-induced
703   renal injury. *JCI Insight* **3**, doi:10.1172/jci.insight.120196 (2018).
704   26   Deis, J. A. *et al.* Adipose Lipocalin 2 overexpression protects against age-related decline
705   in thermogenic function of adipose tissue and metabolic deterioration. *Mol Metab* **24**, 18-
706   29, doi:10.1016/j.molmet.2019.03.007 (2019).
707   27   Ishii, A. *et al.* Obesity-promoting and anti-thermogenic effects of neutrophil gelatinase-
708   associated lipocalin in mice. *Sci Rep* **7**, 15501, doi:10.1038/s41598-017-15825-4 (2017).
709   28   Wang, G. X. *et al.* The brown fat-enriched secreted factor Nrg4 preserves metabolic
710   homeostasis through attenuation of hepatic lipogenesis. *Nat Med* **20**, 1436-1443,
711   doi:10.1038/nm.3713 (2014).
712   29   Maffei, M., Barone, I., Scabia, G. & Santini, F. The Multifaceted Haptoglobin in the
713   Context of Adipose Tissue and Metabolism. *Endocr Rev* **37**, 403-416,
714   doi:10.1210/er.2016-1009 (2016).
715   30   Kumar, K. G. *et al.* Identification of adropin as a secreted factor linking dietary
716   macronutrient intake with energy homeostasis and lipid metabolism. *Cell Metab* **8**, 468-
717   481, doi:10.1016/j.cmet.2008.10.011 (2008).
718   31   Rajbhandari, P. *et al.* Single cell analysis reveals immune cell-adipocyte crosstalk
719   regulating the transcription of thermogenic adipocytes. *Elife* **8**, doi:10.7554/eLife.49501
720   (2019).
721   32   Gargiulo, L. *et al.* A Novel Effect of beta-Adrenergic Receptor on Mammary Branching
722   Morphogenesis and its Possible Implications in Breast Cancer. *J Mammary Gland Biol
723   Neoplasia* **22**, 43-57, doi:10.1007/s10911-017-9371-1 (2017).
724   33   Marchetti, B. *et al.* Beta-adrenergic receptors in the rat mammary gland during pregnancy
725   and lactation: characterization, distribution, and coupling to adenylate cyclase.
726   *Endocrinology* **126**, 565-574, doi:10.1210/endo-126-1-565 (1990).
727   34   Nedvetsky, P. I., Kwon, S. H., Debnath, J. & Mostov, K. E. Cyclic AMP regulates
728   formation of mammary epithelial acini in vitro. *Mol Biol Cell* **23**, 2973-2981,
729   doi:10.1091/mbc.E12-02-0078 (2012).

730   35   Gargiulo, L. *et al.* A Novel Effect of β-Adrenergic Receptor on Mammary Branching
731   Morphogenesis and its Possible Implications in Breast Cancer. *J Mammary Gland Biol*
732   *Neoplasia* **22**, 43-57, doi:10.1007/s10911-017-9371-1 (2017).

733   36   Feng, Y., Manka, D. R., Wagner, K.-U. & Khan, S. A. Estrogen receptor0± expression in
734   the mammary epithelium is required for ductal and alveolar morphogenesis in mice.
735   *Proceedings of the National Academy of Sciences* **104**, 14718 - 14723 (2007).

736   37   Lawson, D. A., Werb, Z., Zong, Y. & Goldstein, A. S. The Cleared Mammary Fat Pad
737   Transplantation Assay for Mammary Epithelial Organogenesis. *Cold Spring Harb Protoc*
738   **2015**, pdb.prot078071, doi:10.1101/pdb.prot078071 (2015).

739   38   Chi, J. *et al.* Three-Dimensional Adipose Tissue Imaging Reveals Regional Variation in
740   Beige Fat Biogenesis and PRDM16-Dependent Sympathetic Neurite Density. *Cell Metab*
741   **27**, 226-236.e223, doi:10.1016/j.cmet.2017.12.011 (2018).

742   39   Centonze, A. *et al.* Heterotypic cell-cell communication regulates glandular stem cell
743   multipotency. *Nature* **584**, 608-613, doi:10.1038/s41586-020-2632-y (2020).

744   40   Bauters, D., Van Hul, M. & Lijnen, H. R. Macrophage elastase (MMP-12) in expanding
745   murine adipose tissue. *Biochim Biophys Acta* **1830**, 2954-2959,
746   doi:10.1016/j.bbagen.2012.12.024 (2013).

747   41   Lee, J. T. *et al.* Macrophage metalloelastase (MMP12) regulates adipose tissue expansion,
748   insulin sensitivity, and expression of inducible nitric oxide synthase. *Endocrinology* **155**,
749   3409-3420, doi:10.1210/en.2014-1037 (2014).

750   42   Shao, M. *et al.* Zfp423 Maintains White Adipocyte Identity through Suppression of the
751   Beige Cell Thermogenic Gene Program. *Cell Metab* **23**, 1167-1184,
752   doi:10.1016/j.cmet.2016.04.023 (2016).

753   43   Gavalda-Navarro, A. *et al.* Lipopolysaccharide-binding protein is a negative regulator of
754   adipose tissue browning in mice and humans. *Diabetologia* **59**, 2208-2218,
755   doi:10.1007/s00125-016-4028-y (2016).

756   44   Sun, W. *et al.* snRNA-seq reveals a subpopulation of adipocytes that regulates
757   thermogenesis. *Nature* **587**, 98-102, doi:10.1038/s41586-020-2856-x (2020).

758   45   Kiefer, F. W. *et al.* Retinaldehyde dehydrogenase 1 regulates a thermogenic program in
759   white adipose tissue. *Nat Med* **18**, 918-925, doi:10.1038/nm.2757 (2012).

760   46   Mina, A. I. *et al.* CalR: A Web-Based Analysis Tool for Indirect Calorimetry Experiments.
761   *Cell Metab* **28**, 656-666 e651, doi:10.1016/j.cmet.2018.06.019 (2018).

762   47   Dobin, A. *et al.* STAR: ultrafast universal RNA-seq aligner. *Bioinformatics* **29**, 15-21,
763   doi:10.1093/bioinformatics/bts635 (2013).

764   48   Kim, D., Langmead, B. & Salzberg, S. L. HISAT: a fast spliced aligner with low memory
765   requirements. *Nat Methods* **12**, 357-360, doi:10.1038/nmeth.3317 (2015).

766   49   Love, M. I., Anders, S., Kim, V. & Huber, W. RNA-Seq workflow: gene-level exploratory
767   analysis and differential expression. *F1000Res* **4**, 1070,
768   doi:10.12688/f1000research.7035.1 (2015).

769   50   Hafemeister, C. & Satija, R. Normalization and variance stabilization of single-cell RNA-
770   seq data using regularized negative binomial regression. *Genome Biol* **20**, 296,
771   doi:10.1186/s13059-019-1874-1 (2019).

772   51   Butler, A., Hoffman, P., Smibert, P., Papalexi, E. & Satija, R. Integrating single-cell
773   transcriptomic data across different conditions, technologies, and species. *Nature*
774   *Biotechnology* **36**, 411-420, doi:10.1038/nbt.4096 (2018).

775 52 Stuart, T. *et al.* Comprehensive Integration of Single-Cell Data. *Cell* **177**, 1888-
776 1902.e1821, doi:10.1016/j.cell.2019.05.031 (2019).
777 53 McInnes, L., Healy, J. & Melville, J. UMAP: Uniform Manifold Approximation and
778 Projection for Dimension Reduction. *arXiv* (2018).
779 54 van der Maaten, L. & Hinton, G. Visualizing Data using t-SNE. *J Mach Learn Res*, 2579-
780 2605 (2008).
781 55 Blondel, V. D., Guillaume, J.-L., Lambiotte, R. & Lefebvre, E. Fast unfolding of
782 communities in large networks. *J. Stat. Mech.* **2008**, P10008, doi:10.1088/1742-
783 5468/2008/10/P10008 (2008).
784 56 Broad Institute. *Study: Mouse Adipose Stromal Vascular Fraction*,
785 <https://singlecell.broadinstitute.org/single_cell/study/SCP708/mouse-adipose-stromal-
786 vascular-fraction#study-summary> (
787 57 Bach, K. *et al.* Differentiation dynamics of mammary epithelial cells revealed by single-
788 cell RNA sequencing. *Nature Communications* **8**, 2128, doi:10.1038/s41467-017-02001-5
789 (2017).
790 58 Guo, G. MCA DGE Data. *Figshare*, doi:10.6084/m9.figshare.5435866.v8 (2020).
791 59 Han, X. *et al.* Mapping the Mouse Cell Atlas by Microwell-Seq. *Cell* **172**, 1091-
792 1107.e1017, doi:10.1016/j.cell.2018.02.001 (2018).
793 60 Tabula Muris: Transcriptomic characterization of 20 organs and tissues from Mus
794 musculus at single cell resolution.
795 61 Tabula Muris Senis.
796 62 Kanehisa, M. & Goto, S. KEGG: Kyoto Encyclopedia of Genes and Genomes. *Nucleic
797 Acids Res* **28**, 27-30, doi:10.1093/nar/28.1.27 (2000).
798 63 Jassal, B. *et al.* The Reactome Pathway Knowledgebase. *Nucleic Acids Res* **48**, D498-
799 D503, doi:10.1093/nar/gkz1031 (2020).
800 64 Nishimura, D. BioCarta. *Biotech Software & Internet Report* **2**, 117-120,
801 doi:10.1089/152791601750294344 (2001).
802 65 Ashburner, M. *et al.* Gene Ontology: tool for the unification of biology. *Nat Genet* **25**, 25-
803 29, doi:10.1038/75556 (2000).
804 66 Alvarsson, A. *et al.* Optical Clearing and 3D Analysis Optimized for Mouse and Human
805 Pancreata. *Bio Protoc* **11**, e4103, doi:10.21769/BioProtoc.4103 (2021).
806 67 Jardé, T. *et al.* Wnt and Neuregulin1/ErbB signalling extends 3D culture of hormone
807 responsive mammary organoids. *Nature Communications* **7**, 13207,
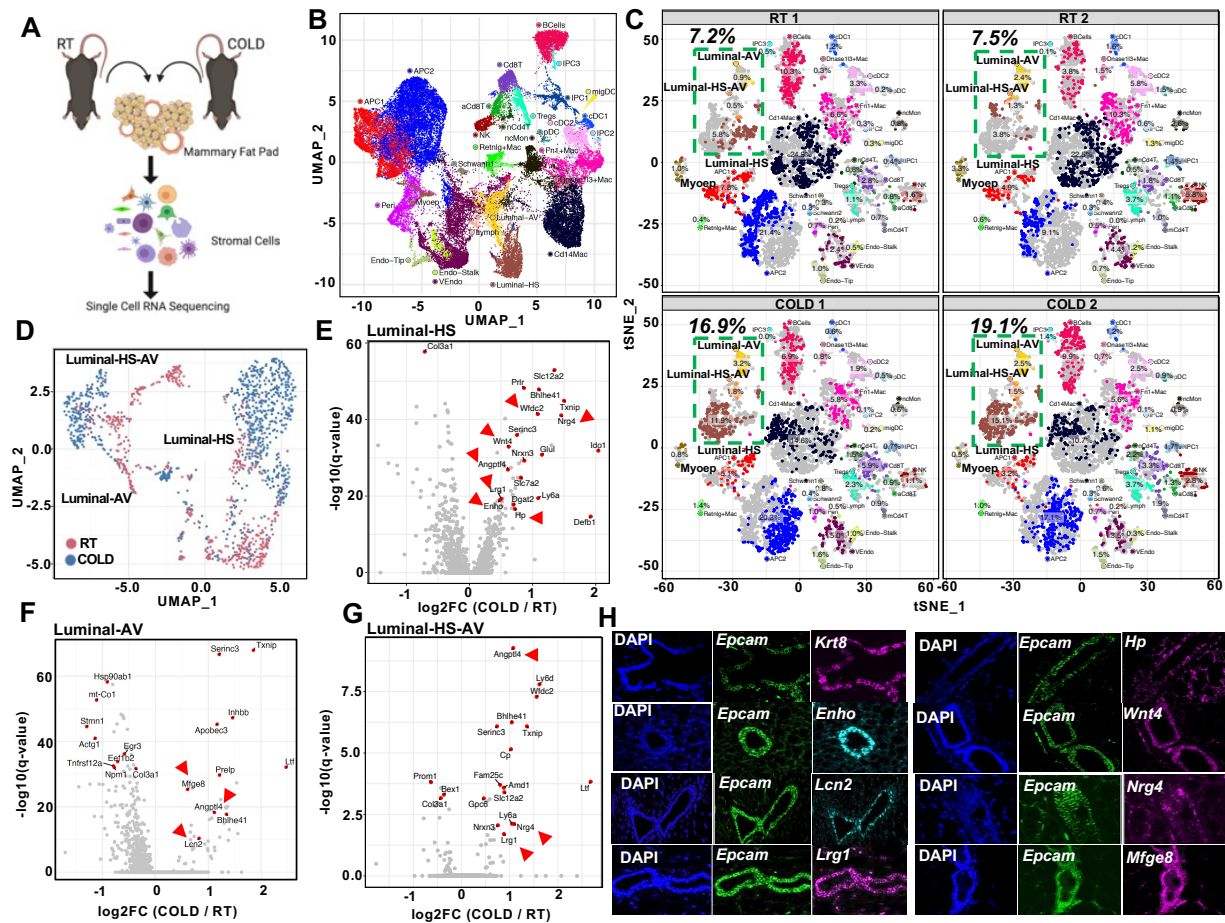808 doi:10.1038/ncomms13207 (2016).
809

810

811

812

813

814

Main Figure 1

Figure 1. Deconstruction of mgWAT shows cold-induced remodeling of mammary epithelium

(A) Cartoon depiction of the scRNA-seq workflow showing isolation of stromal vascular fraction (stromal cells) from mammary fat pad (mgWAT) of 10-week-old 24 h RT or COLD exposed female mice. **(B)** UMAP plots of integrated single cell data from this study and 8 external datasets (see Methods). Each point represents a single cell and clusters are colored by cell type**. (C)** t-SNE plot of single cells from mammary gland and surrounding SVF colored by cell type and separated by sample. Relative fractions of each cell type in each sample are indicated on each cluster. Room temperature (RT) samples are on the top row and 4°C (COLD) are on the bottom row. **(D)** UMAP

plot of luminal epithelial cell types from RT or cold mgWATs. **(E-G)** Differentially expressed

genes between COLD treated mice and RT animals across Luminal-HS (E), Luminal-AV (F), and

Luminal-HS-AV (G). Select significant DEGs (adjusted p-value < 0.05) are highlighted with the

average log fold change between 4 degree and RT indicated on the y-axis. Genes indicated by red

arrows encode for secreted factors. **(H)** RNAScope FISH (see Materials and methods) of indicated

probes from mgWAT of 24 hr cold exposed mice.

Abbreviations: APC, adipose precursor cells; IPC, immune precursor cells; Mac, macrophages;

ncMon, non-classical monocytes; cDC, conventional dendritic cells; migDC, migratory dendritic

cells; pDC, plasmacytoid dendritic cells; Tregs, regulatory T cells; mCd4T, memory Cd4 T cells;

nCd4T, naïve Cd4 T cells; aCd8T, activated Cd8 T cells; Myoep, myoepithelial cells; VEndo,

vascular endothelial cells; Endo-Tip, endothelial tip cells; Endo-Stalk, endothelial stalk cells;

Lymph, lymphatic endothelial cells; Peri, pericytes; Luminal-HS, hormone-sensing luminal cells;

Luminal-AV, secretory alveolar luminal cells; Luminal-HS-AV.
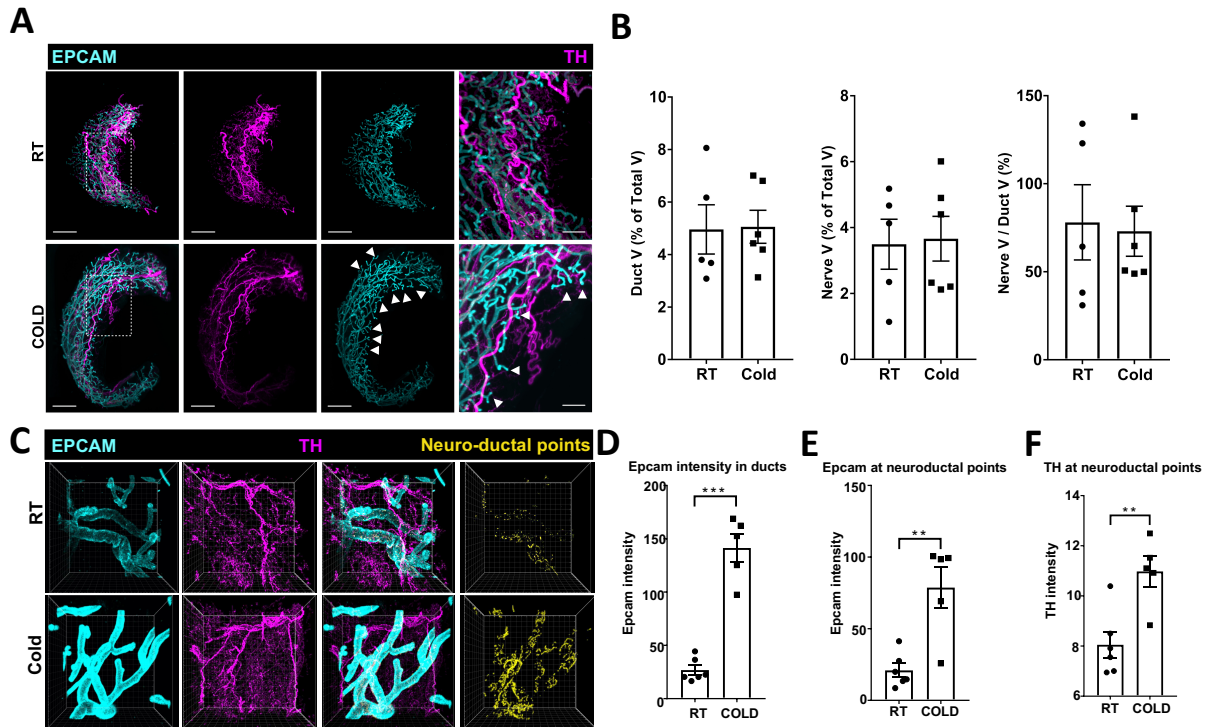
849

850   **Main Figure 2**

851

852

853   **Figure 2. SNS fibers directly innervate mammary ductal epithelium**

854   **(A)** Light sheet microscopy fluorescence (LSFM) images of mgWAT isolated from female mice

855   exposed to RT or COLD for 24 hr and stained with TH antibody (SNS fibers) and EPCAM

856   antibody (ductal cells). Representative mgWAT images from 5-6 mice per condition. White arrows

857   show terminal ductal bifurcations under COLD condition **(B)** Quantification of LSFM images for

858   ductal volume (Duct V) and nerve volume (Nerve V) as a percentage of total volume (Total V),

859   and ratio of Nerve V and Duct V in RT or COLD mgWATs N=5-6 per condition. **(C)** Confocal

860   images of mgWAT isolated from female mice exposed to RT or COLD (24 hr) and stained for

861   EPCAM and TH antibodies. Merged stainings of EPCAM and TH represent neuroductal points.

862   Representative image of 5-6 mice per condition.

863   **(D-F)** Quantification of EPCAM intensity in ducts (D), EPCAM intensity at neuroductal points

864   (E), and TH intensity at neuroductal points (F). N=5-6 per condition. **, $p < 0.01$; ***, $p < 0.001$.

865

866

867

868
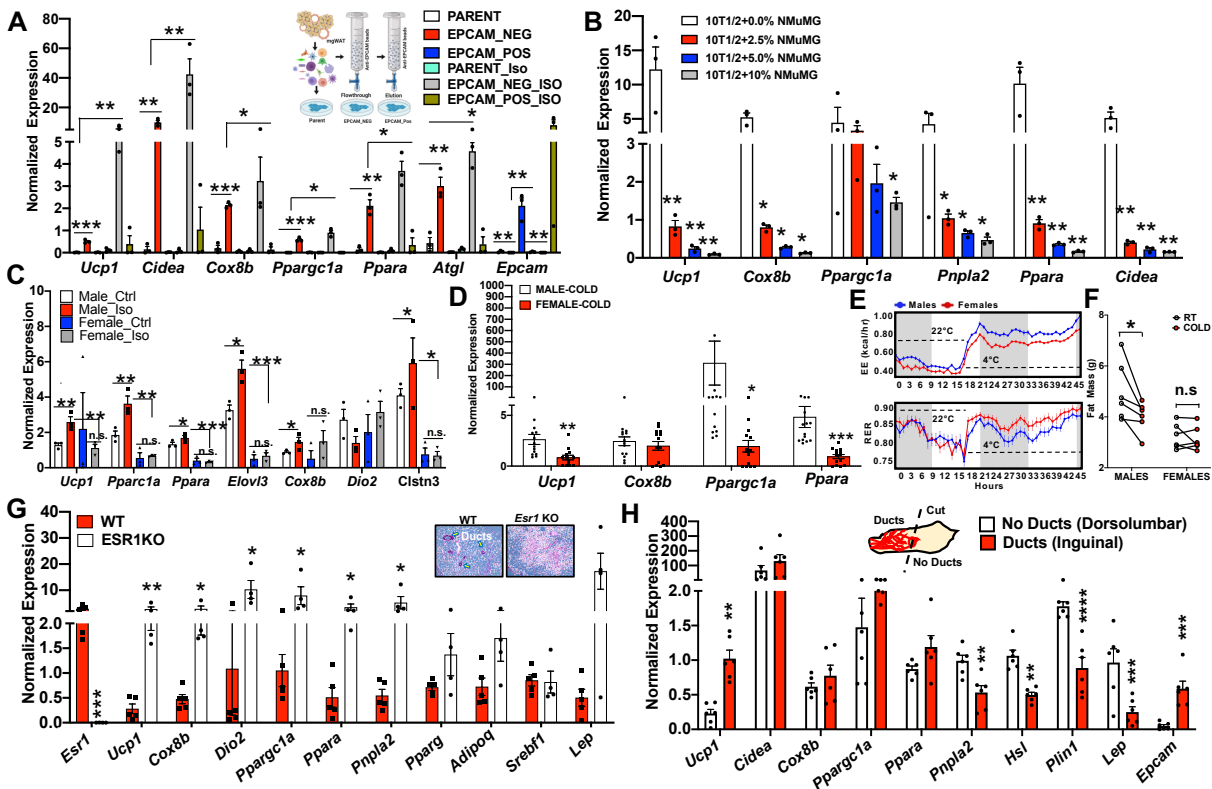
869

870

871

872

873

874

875

876

877

878

879

880

881

882

883

884

885

888

Figure 3. Mammary ductal cells directly inhibit adipocyte thermogenesis.

A) Real-time qPCR of indicated genes from beige differentiation of primary mgWAT SVF (Parent), EPCAM-ve (EPCAM-NEG), and EPCAM+ (EPCAM-POS) cells treated with and without 10 μM isoproterenol (ISO) for 24 hr. Results are from three independent experiments. *, p<0.05**; **, p<0.01; ***, p<0.001. Inset represent a cartoon depiction of selecting and plating EPCAM+ cells from SVFs derived from mgWATs. **B)** Real-time qPCR of indicated genes from beige differentiated and Iso treated 10T1/2 and 2.5-10% NMuMG mixture cells. Results are from three independent experiments. *, p<0.05**; **, p<0.01. **C)** Real-time qPCR of indicated genes from beige differentiated SVFs isolated from male and female iWATs treated with and without Iso. Results are from three independent experiments. *, p<0.05**, **, p<0.01; ***, p<0.001**. **D)** Real-

time qPCR of indicated genes from 24 h cold exposed male and female iWATs. N=13,13 *, p<0.05, **, p<0.01; ***, p<0.001. **E)** Energy expenditure (kcal/hr) and respiratory exchange ratio (RER) of male and female mice exposed to 22°C (21 hr) and 4°C (24 hr) analyzed in Sable Promethion metabolic chambers (12 hr light/dark cycle, 45 hr total duration, white bar represent light cycle and grey bar represent night cycle). N=6,6. **F)** Fat mass of mice from (E) at RT (22°C) and COLD (4°C). N=6,6. *, p<0.05; n.s, not significant. **G)** Real-time qPCR of indicated genes from 24 hr cold exposed WT and *Esr1* KO mgWATs. Inset picture shows histological section of mgWATs from WT and *Esr1* KO mice. Arrows are pointing towards ducts in WT. N=5,5 *, p<0.05, **, p<0.01. **H)** Real-time qPCR of indicated genes from dorsolumbar or inguinal parts of cold-exposed 5-week-old mice. Inset picture shows cartoon depiction of ducts (inguinal) and no ducts (dorsolumbar). Dotted line represents cut site to separate inguinal and dorsolumbar regions of mgWAT. N=6,6. *, p<0.05, **, p<0.01; ***, p<0.001
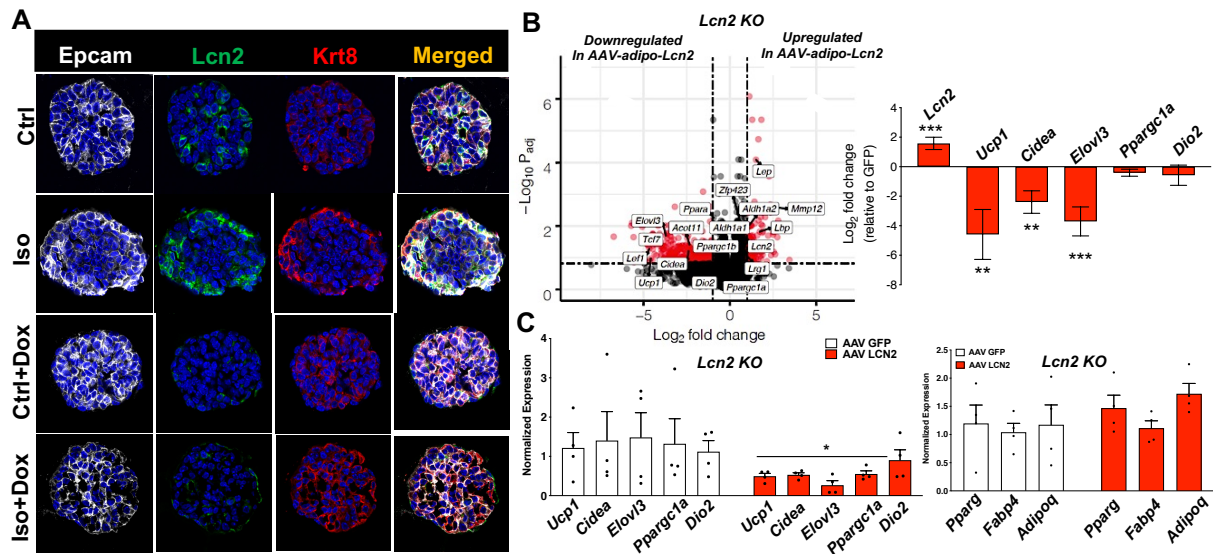
Main Figure 4

Figure 4. LCN2 preserves mgWAT adiposity.

A) Confocal images of immunostaining of indicated antibodies in the organoids derived from K8rtTA-DTA mice (see Methods) treated with and without Iso and Doxycycline (Dox). Representative images from 3 organoid experiments. **B)** Volcano plot of DEGs from the mgWAT of *Lcn2* KO mice treated with adipose-specific AAV-LCN2 or AAV-GFP and represented as a fold change of LCN2/GFP ratio as a function of p-value. Genes labelled are either induced (+) or repressed (-) by Lcn2. **, $p<0.01$; ***, $p<0.001$. N=4,4. **C)** Real-time qPCR of indicated genes from the mgWATs of LCN2KO or WT mice treated with AAV-LCN2 or AAV-GFP. N=4,4. *, $p<0.05$

Extended Data Figure 1
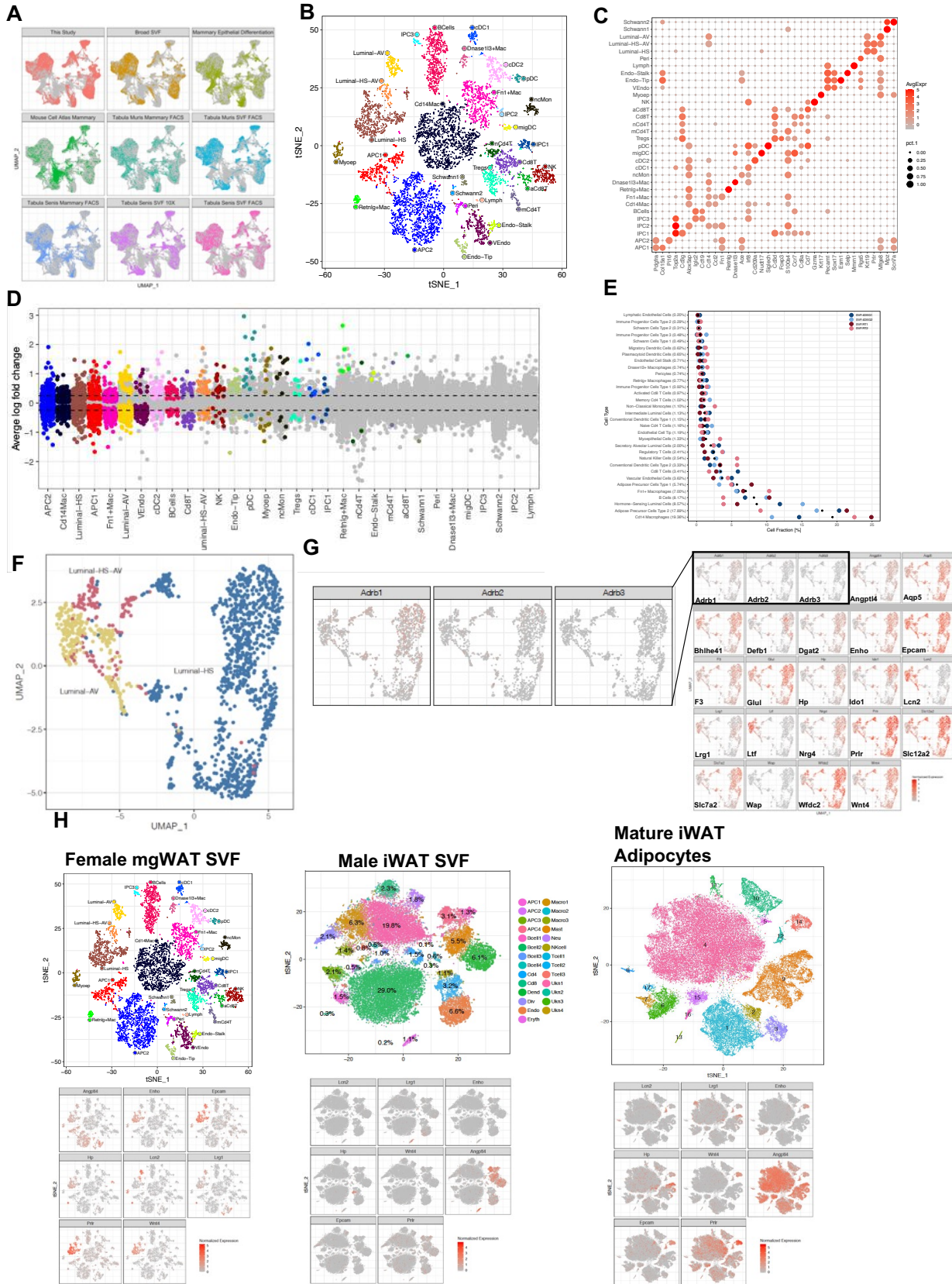
938   **Figure 1. Cold-associated increase in cell percentages of luminal epithelium subtypes.**

939   **A)** UMAP plots of integrated single cell data from this study and 8 external datasets (see Methods

940   and Table 1). Each point represents a single cell and are colored by dataset. **B)** t-SNE plot of single

941   cells from mammary gland and surrounding SVF from this study colored by cell type. Cell types

942   were identified based on expression of canonical marker genes. **C)** Expression of known canonical

943   markers for cell types in the SVF and mammary gland. Color corresponds to average expression

944   level and size corresponds to percentage of cells which express the gene within the cluster. **D)**

945   Differentially expressed genes between COLD (24 hr) treated mice and RT animals across all cell

946   types. Significant DEGs (adjusted p-value < 0.05) are highlighted with the average log fold change

947   between 4 degree and RT indicated on the y-axis. Cell types are ordered on the x-axis based on

948   the number of significant DEGs. **E)** Relative fractions of cell types within each sample. Black dots

949   indicate average relative fractions across all samples. **F)** Aggregated UMAP plot of subclustering

950   of luminal single cells from RT and cold-exposed mice. **G)** UMAP plots of normalized gene

951   expression levels for genes of interest in luminal cells. **H)** tSNE plots of cell type clusters and

952   normalized gene expression levels for genes of interest across multiple datasets including: female

953   mgWAT SVFs, male iWAT SVFs and mature mgWAT adipocytes.
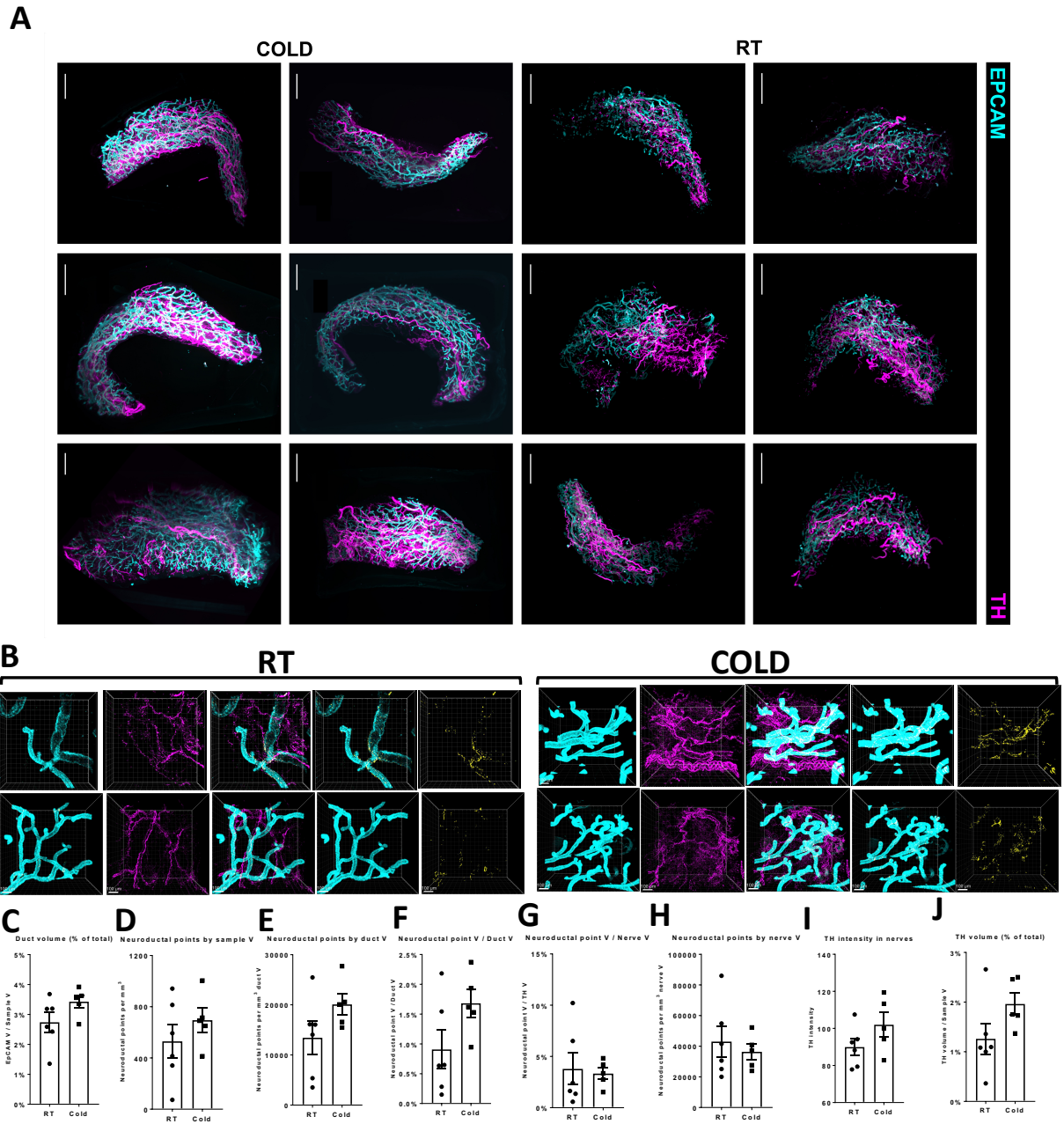
954

955

956

957

958

959

960

Extended Data Figure 2

Figure 2. SNS fibers directly innervate ductal epithelial cells.

964   **A)** Light sheet microscopy fluorescence (LSFM) images of mgWAT isolated from female mice

965   exposed to RT or COLD for 24 hr and stained with TH antibody (SNS fibers) and EPCAM

966   antibody (ductal cells). N=6,6. **B)** Confocal images of mgWAT isolated from female mice exposed

967   to RT or COLD for 24hr and stained for EPCAM and TH antibodies. Merged staining of EPCAM

968   and TH represent neuroductal points. Representative images of 5-6 mice per condition. **C-J)**

969   Quantification of indicated parameters of images from (B). N=5-6 mice per condition.

970

971

972

973

974

975
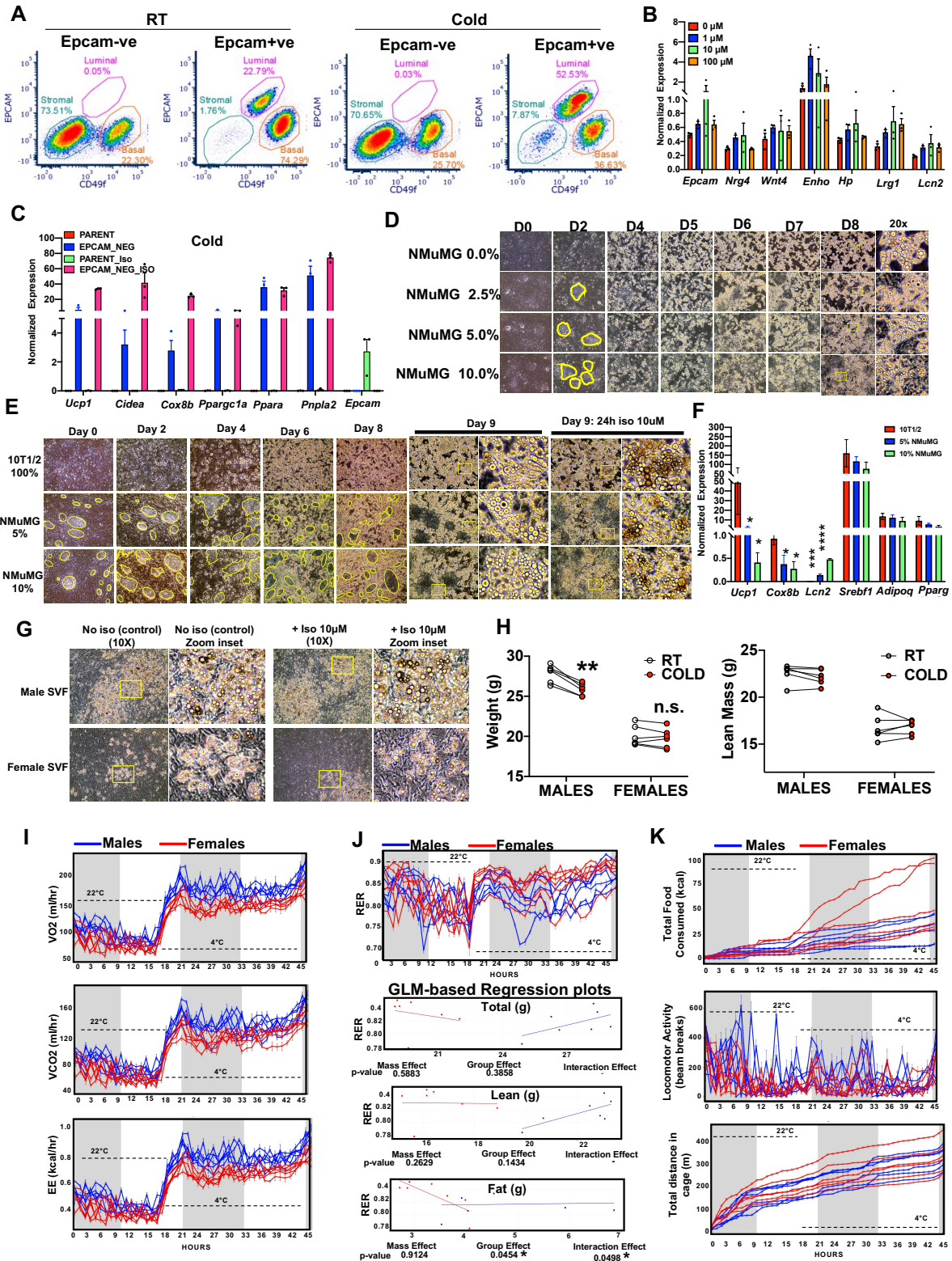
976

977

978

979

980

981

982

983

984

985

986

987

988

989

992 **Figure 3. Mammary gland epithelium inhibits cold-induced adipocyte thermogensis**

993 **A)** Representative FACS plot of CD49f and EPCAM expression in EPCAM bead selected

994 EPCAM+ or EPCAM-ve epithelial cells from RT or cold mice. 2 mice per condition and 4

995 mammary fat pads per mouse. Representative data from 4 independent experiments. **B)** Real-time

996 qPCR of indicated genes in beige differentiated SVFs from mgWAT treated with indicated

997 concentration of Iso for 5 hr. **C)** Real-time qPCR of indicated genes from beige differentiated

998 primary mgWAT SVF (Parent) and EPCAM-ve (EPCAM-NEG) cells isolated from cold exposed

999 mice treated with and without 10 μM isoproterenol (ISO) for 24 hr ex vivo. Results are from three

1000 independent experiments. **D)** Images showing cell morphology of D0-D8 beige differentiated

1001 10T1/2 and NMuMG (0, 5, and 10%) mixture cells. Yellow enclosures show NMuMG epithelial

1002 cells surrounded by 10T1/2 cells. **E)** Images showing cell morphology of D0-D9 beige

1003 differentiated 10T1/2 and NMuMG (0-10%) mixture cells. Yellow enclosures show NMuMG

1004 epithelial cells surrounded by 10T1/2 cells. **F)** Real-time qPCR of indicated genes from cells in

1005 (E). Results are from three independent experiments. *, $p<0.05$, ***, $p<0.001$. **G)** Images showing

1006 cell morphology of beige differentiated SVFs isolated from male and female iWATs. **H)** Body

1007 weight and lean mass of male and female mice before (RT) and after 24 hr cold exposure (COLD).

1008 N=6,6. **, $p<0.01$. **I-K)** Individual mice data for oxygen consumption (VO2 ml/hr), carbon

1009 dioxide production (VCO2 ml/hr), and energy expenditure (EE kcal/hr) (I), respiratory exchange

1010 ratio (RER) and generalized linear model (GLM)-based regression plots of RER with total body

1011 weight (Total), lean mass (Lean) and fat mass (Fat) as co-variates (ANCOVA) showing p-value

1012 for Mass effect, Group effect, and Interaction effect. *, $p<0.05$ (J), and total food consumed (kcal),

1013 locomotor activity (beam breaks), and total distance in cage (m) (K) of male and female mice

1014 exposed to 22°C for 21 hr and 4°C for 24 hr in Sable Promethion metabolic chambers (12 hr

1015 light/dark cycle, 45 hr total duration, white bar represents light cycle and grey bar represents night

1016 cycle). N=6,6.

1017

1018

1019

1020

1021

1022

1023
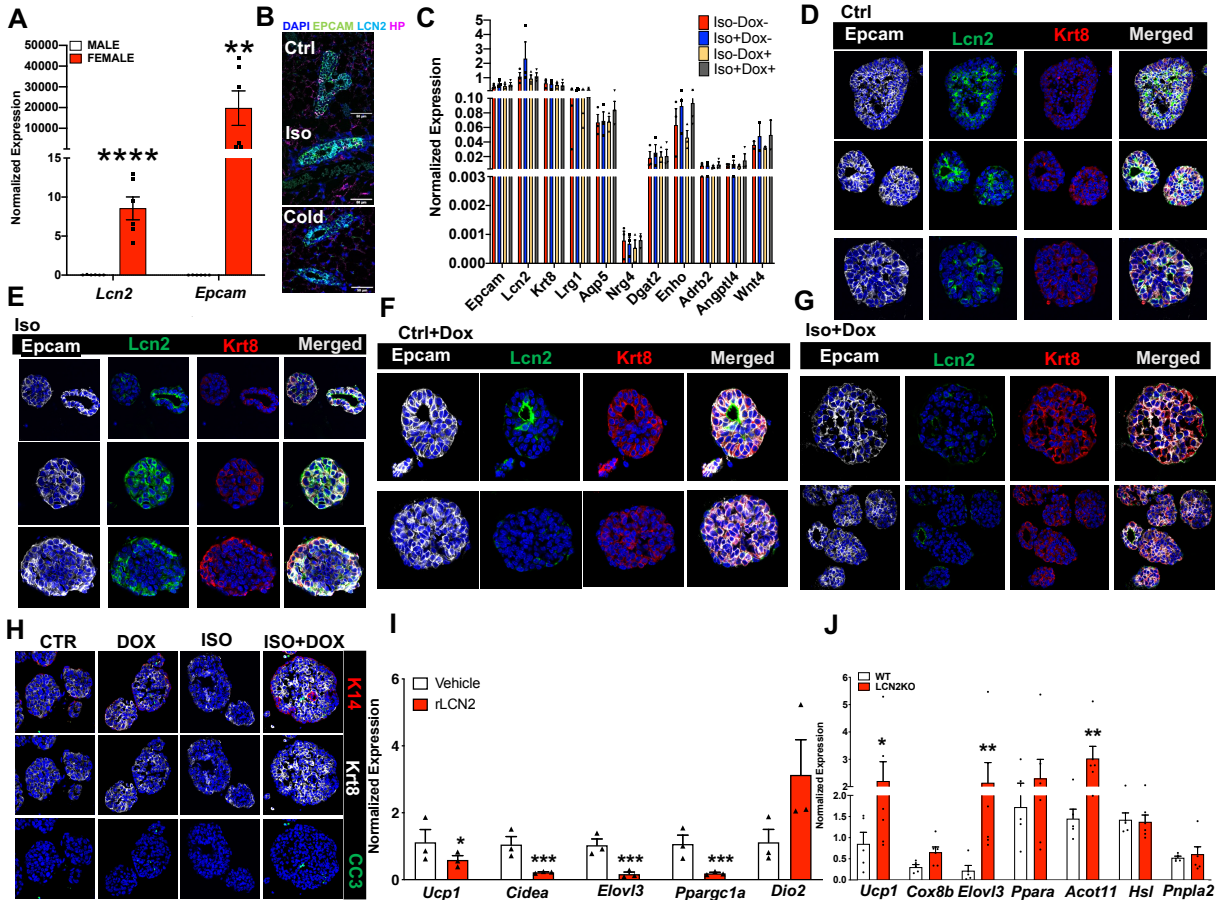
1024

1025

1026

1027

1028

1029

1030

1031

1032

1033

1034

1035

1036

1037

Extended Data Figure 4

1039

1040 **Figure 4. LCN2 is a cold-induced mammokine involved in blocking cold-induced adipocyte**

1041 **UCP1 expression**

1042 **A)** Real-time qPCR of indicated genes from 24 hr cold-exposed male and female iWATs. ****,**

1043 p<0.01; *****,** p<0.001. **B)** RNAScope FISH (see Materials and Methods) of indicated probes from

1044 mgWAT of RT or 24 hr isoproterenol or cold-exposed mice. **C)** Real-time qPCR of indicated genes

1045 in organoids derived from K8rtTA-DTA mice treated with and without ISO and Doxycycline

1046 (Dox). Results from 3 organoid experiments. **D-H)** Confocal images of immunostaining of

1047 indicated antibodies in organoids derived from K8rtTA-DTA mice treated with and without Iso

1048 and Dox. Representative images from 2-3 organoid experiments. **I)** Real-time qPCR of indicated

1049   genes from beige differentiation mgWAT SVFs derived from *Lcn2* KO mice treated with and

1050   without recombinant Lcn2 (rLcn2). *, p<0.05; ***, p<0.001 **J)** Real-time qPCR of indicated genes

1051   from 24 hr cold exposed WT and *Lcn2* KO mgWATs. N=5,5. *, p<0.05; **, p<0.01

1052

1053

1054

1055

1056

1057

1058

1059

1060

1061

1062

1063

1064

1065

1066

1067

Supplementary Files

This is a list of supplementary files associated with this preprint. Click to download.

- SantosNatureMovie1.pptx
- SantosNatureMovie2.pptx
- SupplementaryTable1.xlsx